Dicke superradiance in ordered arrays of multilevel atoms

Stuart J. Masson,[1,*] Jacob P. Covey,[2] Sebastian Will,[1] and Ana Asenjo-Garcia[1,†]

[1] *Department of Physics, Columbia University, New York, NY 10027, USA*
[2] *Department of Physics, The University of Illinois at Urbana-Champaign, Urbana, IL 61801, USA*

(Dated: April 4, 2023)

In fully-inverted atomic ensembles, photon-mediated interactions give rise to Dicke superradiance, a form of many-body decay that results in a rapid release of energy as a photon burst. While originally studied in point-like ensembles, this phenomenon persists in extended ordered systems if the inter-particle distance is below a certain bound. Here, we investigate Dicke superradiance in a realistic experimental setting using ordered arrays of alkaline earth(-like) atoms, such as strontium and ytterbium. Such atoms offer exciting new opportunities for light-matter interaction as their internal structure offers the possibility of trapping at short interatomic distances compared to their strong long-wavelength transitions, providing the potential for strong collectively modified interactions. Despite their intricate electronic structure, we show that two-dimensional arrays of these atomic species should exhibit many-body superradiance for achievable lattice constants. Moreover, superradiance effectively "closes" transitions, such that multilevel atoms become more two-level like. This occurs because the avalanche-like decay funnels the emission of most photons into the dominant transition, overcoming the single-atom decay ratios dictated by their fine structure and Zeeman branching. Our work represents an important step in harnessing alkaline-earth atoms as quantum optical sources and as dissipative generators of entanglement.

I. INTRODUCTION

Atoms in a cavity emit into the same electromagnetic mode, leading to interactions between them, and a collective interaction between light and matter. Interactions are well understood within the paradigm of cavity quantum electrodynamics (QED), as the indistinguishability of the atoms enables their description as a large spin coupled to a single radiative channel. An emblematic example of many-body physics in cavity QED is Dicke superradiance [1–5], where fully-inverted atoms decay by radiating light in a short bright pulse with peak intensity that scales quadratically with atom number [see Fig. 1(a)]. Dicke superradiance has also been observed in Bose-Einstein condensates [6–8], where a macroscopically-occupied state couples to light. In these scenarios, superradiance is well understood because the permutational symmetry arising from indistinguishability restricts dynamics to a small subspace of the full Hilbert space.

Understanding collective light-matter interactions beyond the cavity QED regime is critical not only from a fundamental point of view, but also to realize applications in quantum non-linear optics, quantum simulation, and metrology. Potentially, one could translate concepts such as the superradiant laser [9, 10], driven-dissipative phase transitions [11, 12], and quantum-enhanced sensing [13–15] into a much larger class of systems. For instance, atomic arrays in the single-excitation regime have been proposed as promising platforms for generating novel light sources and optical components, with the recent realization of an atomically-thin mirror [16, 17] as an example. The many-body landscape offers a far greater toolbox, and could open up possibilities to create sources of light with unusual statistical properties [18–23] or to generate entangled atomic states via dissipation [24–32].

In extended systems in free space, interactions between atoms depend on their relative positions. Theoretical studies of Dicke superradiance in this regime have been greatly limited, as the broken permutational symmetry increases the complexity of the problem, which in principle scales exponentially with atom number. However, experiments have confirmed that superradiant bursts can still occur. The first demonstrations occurred in thermal molecular and atomic vapors [33–37], but observations have since been made in several other systems [38–41]. In contrast to other phenomena (such as subradiance), superradiance is attractive from an experimental point of view, as it is robust under many imperfections and does not require single photon detection.

Ordered atomic arrays [42–47] have been recently suggested as a promising platform to study many-body decay [27, 48–51]. In contrast to other setups that typically suffer from dephasing arising from thermal motion or coherent (i.e., Hamiltonian) dipole-dipole interactions, atomic arrays are supposed to experience less dephasing, as the role of Hamiltonian dipole-dipole interactions in the burst is significantly reduced due to the spatial order. In these systems, atoms can decay into many radiative channels. Nevertheless, it has been shown that signatures of superradiance should persist in very extended two-dimensional (2D) systems, of size much larger than the transition wavelength [48–50].

Here, we propose the use of alkaline earth(-like) atoms (AEAs) in atomic arrays to observe and control Dicke superradiance. These atoms have favorable transitions that enable their trapping at relatively small distances in comparison to the wavelength of the emitted photons.

* s.j.masson@columbia.edu
† ana.asenjo@columbia.edu

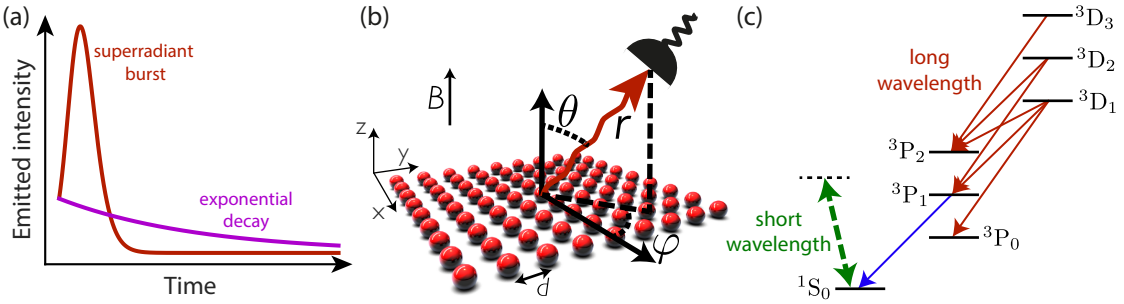

FIG. 1. (a) Atoms at a point emit a superradiant burst, with a peak intensity that scales as the square of the number of atoms, in contrast to uncorrelated atoms, which emit an exponentially-decaying pulse. (b) Schematics of the proposed setup: A 2D array of N atoms with lattice constant d is held in the $x-y$ plane with quantization axis set by a magnetic field along the z-axis. Light is measured in the far field, at a location described by spherical coordinates $\{r, \theta, \varphi\}$, where $r \gg \sqrt{N}d$. (c) Relevant level structure of bosonic AEAs. The atoms are optically trapped via strong transitions at short wavelengths (dashed line). The atoms are then prepared in a $^3\mathrm{D}_J$ state, where they decay to $^3\mathrm{P}_J$ states emitting light with a (relatively long) infrared wavelength, and then potentially decay further to the $^1\mathrm{S}_0$ state. Possible decay paths are indicated by solid lines. Due to the difference in wavelengths, decay dynamics from $^3\mathrm{D}_J$ will be dictated by many-body effects.

While the atoms are intrinsically multilevel in nature, we demonstrate that the internal competition presented by the different transitions does not prohibit Dicke superradiance. Via a cumulant expansion, we approximate the dynamics and compute the superradiant bursts that would be emitted by arrays of lattice constants that can be achieved in state-of-the-art experimental setups. The emitted light is nontrivially dependent on the geometry of the array and detector location [as shown in Fig. 1(b)]. For example, as the interatomic distance is increased, the superradiant burst is lost but then reappears. We show that this dependence can be easily predicted by the use of conditional two-photon correlation functions. Finally, we show how to use Dicke superradiance to inhibit or enhance decay into a particular state, overcoming limits set by fine structure and Zeeman branching. This work suggests that AEAs offer significant advantages for exploring and harnessing superradiance in atom arrays.

The paper is structured as follows. In Section II, we introduce the full relevant structure of AEAs. In Section III, we consider toy models of multi-level atoms at a single spatial location. We show that Dicke superradiance occurs both for decay to multiple ground states and for cascaded decay (i.e., where the excited state decays to intermediate states before decaying to the final ground state). This allows us to simplify the full level structure of AEAs, keeping only relevant transitions. In Section IV, we introduce the methods necessary to treat these simplified AEAs in ordered arrays with finite separation. In Section V, we show that significant bursts can be achieved in reasonably sized arrays of AEAs, and that this decay can be tailored via the lattice constant.

II. TRANSITIONS OF ALKALINE EARTH ATOMS

Here, we discuss the relevant atomic transitions of AEAs. These bielectron species have different wavelength transitions that, in theory, allow for trapping and cooling on a short wavelength and for realizing quantum optics experiments on a much longer wavelength [58] [see Fig. 1(c)]. In particular, the $^1\mathrm{S}_0$ and metastable $^3\mathrm{P}_{\{0,2\}}$ states can be trapped at an optical wavelength. If the atoms are excited into a state in the $^3\mathrm{D}_J$ manifold, decay occurs at infrared wavelengths, relative to which the atoms have significantly subwavelength spacing. We consider the bosonic isotopes ^{88}Sr and ^{174}Yb, where there is

transition	wavelength (nm)	decay rate ($\times 10^6$ s^{-1})
$^3\mathrm{P}_1 \to {}^1\mathrm{S}_0$	556 [52]	1 [53]
$^3\mathrm{D}_1 \to {}^3\mathrm{P}_0$	1389 [52]	2 [53]
$^3\mathrm{D}_1 \to {}^3\mathrm{P}_1$	1540 [52]	1 [53]
$^3\mathrm{D}_1 \to {}^3\mathrm{P}_2$	2090 [52]	0.03 [53]
$^3\mathrm{D}_2 \to {}^3\mathrm{P}_1$	1480 [52]	2 [53]
$^3\mathrm{D}_2 \to {}^3\mathrm{P}_2$	1980 [52]	0.3 [53]
$^3\mathrm{D}_3 \to {}^3\mathrm{P}_2$	1800 [52]	2 [53]

TABLE I. Wavelengths and decay rates for relevant transitions in ^{174}Yb.

transition	wavelength (nm)	decay rate ($\times 10^5$ s^{-1})
$^3\mathrm{P}_1 \to {}^1\mathrm{S}_0$	689 [54]	0.47 [54]
$^3\mathrm{D}_1 \to {}^3\mathrm{P}_0$	2600 [55]	2.8 [56]
$^3\mathrm{D}_1 \to {}^3\mathrm{P}_1$	2740 [55]	1.8 [56]
$^3\mathrm{D}_1 \to {}^3\mathrm{P}_2$	3070 [55]	0.088 [56]
$^3\mathrm{D}_2 \to {}^3\mathrm{P}_1$	2690 [55]	3.3 [54]
$^3\mathrm{D}_2 \to {}^3\mathrm{P}_2$	3010 [55]	0.79 [54]
$^3\mathrm{D}_3 \to {}^3\mathrm{P}_2$	2920 [55]	5.9 [57]

TABLE II. Wavelengths and decay rates for relevant transitions in ^{88}Sr.

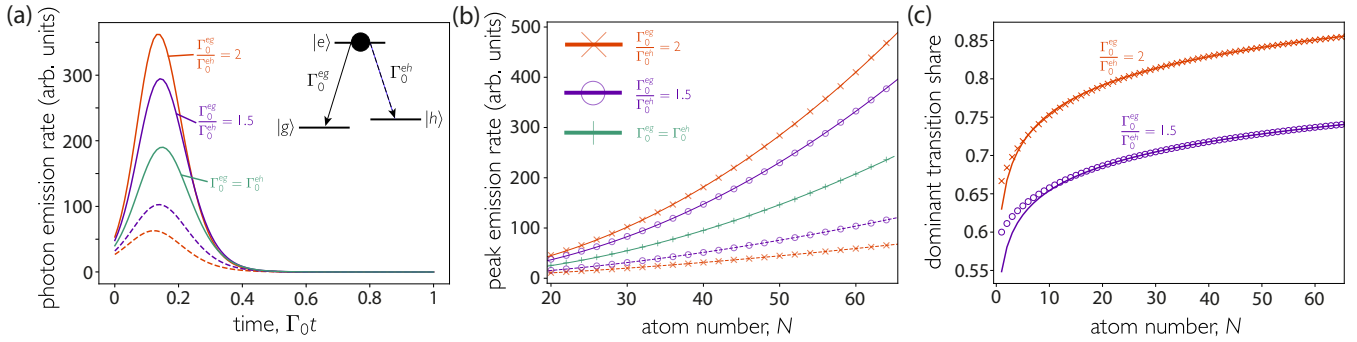

FIG. 2. Superradiant decay from Λ-atoms at a point. Each atom decays at a total rate $\Gamma_0 = \Gamma_0^{eg} + \Gamma_0^{eh}$ split between two levels. (a) Superradiant bursts emitted by 40 Λ-atoms. Solid lines indicate emission on the brighter transition $|e\rangle \to |g\rangle$, while dashed lines indicate emission on the less bright transition $|e\rangle \to |h\rangle$. (b) Scaling of the peak emission on each transition. Solid lines are power-law best fits of data from $N \geq 20$. Solid fit lines indicate a brighter transition, while dashed fit lines indicate a less bright transition. The scalings are $\sim N^{2.01}$ and $\sim N^{2.00}$ for the brighter transitions with $\Gamma_0^{eg} = 2\Gamma_0^{eh}$ and $\Gamma_0^{eg} = 1.5\Gamma_0^{eh}$ respectively, while the less bright transitions scale as $N^{1.56}$ and $N^{1.72}$. In the balanced case, the scaling is $N^{1.92}$ for both pathways. (c) Fraction of photons emitted on the brighter transition. Solid lines are lines of best fit of data from $N \geq 20$ of the form $A\ln(N) + B$. For $\Gamma_0^{eg} = 2\Gamma_0^{eh}$, the fit is $0.054\ln(N) + 0.630$. For $\Gamma_0^{eg} = 1.5\Gamma_0^{eh}$, the fit is $0.046\ln(N) + 0.549$.

no nuclear spin and thus no hyperfine splitting, for the sake of simplicity. Results can be extended to fermionic isotopes, where similar physics should be observable.

The internal structure of AEAs is well characterized due to their excellent performance as optical atomic clocks [59–67]. In recent years, AEA arrays have also attracted much attention as candidates for quantum computing [68–71], with significant advancements with both strontium [72–74] and ytterbium [75–78]. Current tweezer array implementations use Rydberg states to mediate interactions, and do not require subwavelength spacing. Nevertheless, quantum gas microscopes of ^{174}Yb have been demonstrated, with interatomic spacings of 266 nm [79, 80].

^{174}Yb can be operated as an optical source at telecom wavelengths, as the $^3\mathrm{D}_1 \to {}^3\mathrm{P}_{\{0,1\}}$ and $^3\mathrm{D}_2 \to {}^3\mathrm{P}_1$ transitions have wavelengths of around $1.4 - 1.5$ μm. Therefore, the light emitted on these transitions is compatible with low-loss fiber-optic cables and devices built with these atoms can be integrated into distributed photonic networks without need for quantum frequency conversion [81–83]. Alternatively, two-level systems can be found on the $^3\mathrm{D}_3 \to {}^3\mathrm{P}_2$ line. In addition, lasers and optical components are readily available for all these transitions. Full details of the transition wavelengths and decay rates for ytterbium are given in Table I.

In ^{88}Sr the ratio between trapping and science wavelengths is even more beneficial to realize closely-packed arrays. In particular, atoms initialized in the $^3\mathrm{D}_3$ state decay at a wavelength of 2.9 μm. However, these transitions are in the mid-infrared, where sources, detectors and other components are less readily available. Full details of the transition wavelengths and decay rates for strontium are given in Table II.

Longer wavelength transitions also exist in alkali atoms, including at telecom frequencies [84–87]. However, the lack of metastable states means the needed initial state is more difficult to prepare. Furthermore, intermediate states have significantly larger linewidths, such that the simplifications we make to the level structure for AEAs are not necessarily valid for alkalis. Additionally, the relatively small fine and hyperfine splitting combined with large multiplicity yields a cluttered spectrum.

III. MULTILEVEL ATOMS AT A POINT

We first consider a toy model where atoms are all at the same spatial location and are initially in the excited state. This endows the system with enough symmetry that exact dynamics can be calculated for large atom number. It is well established that superradiance can still occur if there are multiple ground states [30, 88, 89]. Here, we show how the properties of the decay change with atom number, allowing us to simplify the level structure of the considered AEAs in Section V.

If all atoms are at a point or, equivalently, identically coupled to a cavity mode, they are indistinguishable. Their indistinguishability means that there is no Hamiltonian interaction and decay is diagonalized into the action of symmetric spin lowering operators of the form $\hat{S}_{ge} = \sum_{j=1}^{N} \hat{\sigma}_{ge}^{j}$ where $\hat{\sigma}_{ge}^{j} = |g\rangle_j \langle e|_j$ is the lowering operator between states $|e\rangle$ and $|g\rangle$ for atom j. The complexity of this problem scales as $\mathcal{O}(N^{m-1})$ for m-level atoms, making use of the permutational symmetry and conserved total atom number.

A. Multiple ground states: Λ-systems

We now consider a Λ-system where the excited state can decay to two different ground states. The frequencies of these transitions are assumed to be far separated such

that the channels are independent. In the limit of atoms at a point, the dynamics follows the master equation

$$\dot{\rho} = \Gamma_0^{eg}\ell[\hat{S}_{ge}](\rho) + \Gamma_0^{eh}\ell[\hat{S}_{he}](\rho), \tag{1}$$

where decay is diagonalized into collective lowering operators $\hat{S}_{ge,he} = \sum_{j=1}^{N}\hat{\sigma}^j_{ge,he}$ and

$$\ell[\hat{A}](\rho) = \hat{A}\rho\hat{A}^\dagger - \frac{1}{2}\hat{A}^\dagger\hat{A}\rho - \frac{1}{2}\rho\hat{A}^\dagger\hat{A}. \tag{2}$$

Superradiant bursts can be emitted on multiple channels at the same time, as shown in Fig. 2. Both the height of the burst and its scaling with N depend on the relative strength of the decay channels. For channels of equal decay rate, $\Gamma_0^{eg} = \Gamma_0^{eh}$, the best fit for the peaks' scaling is $N^{1.92}$, instead of the N^2 scaling for two-level systems at a point. For imbalanced channels, $\Gamma_0^{eg} > \Gamma_0^{eh}$, the larger burst scales faster than for balanced channels. For the relative rates of decay of $2:1$ and $1.5:1$, the best-fit scalings of the peak intensity emitted on the stronger transition are $N^{2.01}$ and $N^{2.00}$ respectively. This implies that in such configurations, as long as there is some bias towards one transition, for large enough N, the peak on that transition will always scale as the ideal two-level case with N^2. In the case of balanced channels, neither channel gains any advantage, and so the scaling is reduced. Furthermore, the superradiant burst on the weaker transition has a peak that scales slower than the balanced case. For $\Gamma_0^{eg} = 2\Gamma_0^{eh}$, the scaling is $N^{1.56}$ and for $\Gamma_0^{eg} = 1.5\Gamma_0^{eh}$ it is $N^{1.72}$.

The percentage of photons emitted on the bright channel increases logarithmically with atom number, as shown in Fig. 2(c). Significant population accumulates in $|g\rangle$ faster than in $|h\rangle$, and so the collective enhancement of Dicke superradiance occurs earlier, "stealing" photons from the weaker transition. For large atom number, if the ratio between decay rates is strongly biased towards the brighter transition, the impact of the weaker transition is minimal. The bias of the imbalance of photons emitted on each transition was reported in Ref. [30].

B. Cascaded decay: Ladder-systems

We now consider a ladder system where the excited state, $|e\rangle$, decays to an intermediate state $|f\rangle$, that itself decays again to the ground state $|g\rangle$. In the limit of all atoms at a point, dynamics follows the master equation

$$\dot{\rho} = \Gamma_0^{ef}\ell[\hat{S}_{ef}](\rho) + \Gamma_0^{fg}\ell[\hat{S}_{fg}](\rho), \tag{3}$$

where decay is diagonalized into collective lowering operators $\hat{S}_{ef,fg} = \sum_{j=1}^{N}\hat{\sigma}^j_{ef,fg}$.

A superradiant burst is emitted on both transitions consecutively, as shown in Fig. 3(b). This is because the excited state decay is extremely fast due to large population inversion, while the decay of the intermediate state is very small due to small inversion. By the time

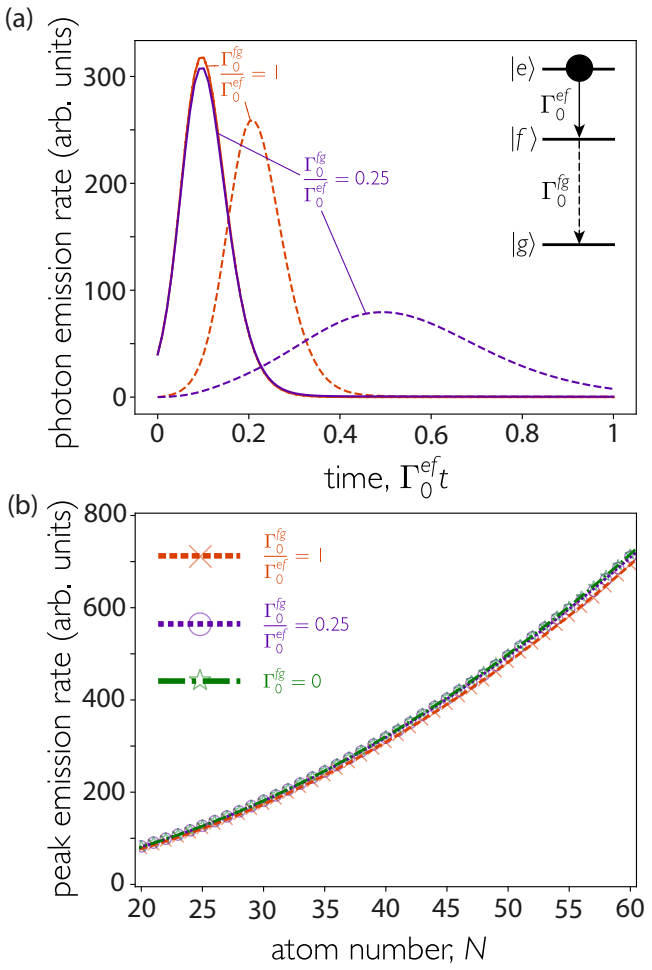

FIG. 3. Superradiant decay from ladder-atoms at a point. Each atom decays initially at a rate Γ_0^{ef} to an intermediate state which itself decays at a rate Γ_0^{fg}. (a) Superradiant bursts emitted by 40 ladder atoms. Solid (dashed) lines indicate emission on the initial (secondary) transition. (b) Scaling of the peak emission by N ladder atoms. Lines are power-law best fits of data from $N \geq 20$. In all three cases the fit scales as approximately N^2.

that the population in the intermediate state is large enough to drive fast collective decay, the superradiant burst from the first transition is mostly finished. In the regime $N\Gamma_0^{ef} \gg \Gamma_0^{fg}$, the scaling of the first superradiant peak goes approximately as $\sim N^2$ regardless of the relative ratio of decays and the two-level case is retrieved.

IV. THEORETICAL METHODS FOR ORDERED EXTENDED ARRAYS

A. Spin model for multilevel atoms

Here we introduce the theoretical framework to investigate an array of N multilevel atoms that interact with

each other via free space beyond the point approximation. Without permutational symmetry, atoms interact both coherently and dissipatively. Under a Born-Markov approximation, the atomic density matrix evolves according to the master equation [90, 91]

$$\dot{\rho} = \sum_a -\frac{\mathrm{i}}{\hbar}[\mathscr{H}_a, \rho] + \mathscr{L}_a(\rho), \tag{4}$$

where an excited state $|e\rangle$ decays to a set of ground states $|g_a\rangle$. Each Hamiltonian and Lindbladian read

$$\mathscr{H}_a = -\hbar\omega_a \sum_{j=1}^{N} \hat{\sigma}^j_{g_a g_a} + \sum_{j,l=1}^{N} J^a_{jl} \hat{\sigma}^j_{e g_a} \hat{\sigma}^l_{g_a e}, \tag{5}$$

$$\mathscr{L}_a(\rho) = \sum_{j,l=1}^{N} \frac{\Gamma^a_{jl}}{2} \left(2\hat{\sigma}^j_{g_a e}\rho\hat{\sigma}^l_{e g_a} - \hat{\sigma}^j_{e g_a}\hat{\sigma}^l_{g_a e}\rho - \rho\hat{\sigma}^j_{e g_a}\hat{\sigma}^l_{g_a e}\right), \tag{6}$$

where ω_a is the frequency of the transition from $|e\rangle \to |g_a\rangle$, $\hat{\sigma}^j_{g_a e} = |g_a\rangle_j \langle e|_j$ is the lowering operator from state $|e\rangle \to |g_a\rangle$ for the jth atom, and interactions between atoms j and l are characterized by

$$J^a_{jl} - \frac{\mathrm{i}\Gamma^a_{jl}}{2} = -\frac{\mu_0\omega_a^2}{\hbar} \boldsymbol{\wp}^*_a \cdot \mathbf{G}_0(\mathbf{r}_j, \mathbf{r}_l, \omega_a) \cdot \boldsymbol{\wp}_a. \tag{7}$$

Here, $\boldsymbol{\wp}_a$ is the normalized dipole matrix element of the transition, and $\mathbf{G}_0(\mathbf{r}_j, \mathbf{r}_l, \omega_a)$ is the electromagnetic field propagator between atoms at positions $\mathbf{r}_j$ and $\mathbf{r}_l$ [92].

Throughout the manuscript, we consider that the transition frequencies are all sufficiently distinct such that photons associated with one transition cannot excite any others, and interactions of the form $\hat{\sigma}^j_{e g_a}\hat{\sigma}^l_{g_b e}$ are heavily detuned and can be ignored. This condition is naturally met for transitions from an excited state to states with different angular momentum. For transitions to different Zeeman levels, we assume the presence of a magnetic field to break the degeneracy. This requires the Zeeman splitting to be much larger than the linewidth of the emitted light. The spectrum is maximally broadened for two-level atoms at the same spatial location, as this situation produces the shortest possible burst. In this case, one requires a magnetic field with $B \gg N\Gamma_0/\mu_B$, where Γ_0 is the bare decay rate of a single atom. This corresponds to magnetic fields on the order of ~ 100G for the atom numbers considered here. For 2D arrays, the power spectrum is expected to scale sub-linearly with atom number, thus requiring smaller Zeeman shifts.

B. Conditions for many-body superradiance

1. Two level systems

The emission of a superradiant burst can be predicted using the set of eigenvalues of the dissipative interaction matrix $\mathbf{\Gamma}$ with elements Γ^{jl}, $\{\Gamma_\nu\}$ [48]. The minimal requirement for a superradiant burst is an initial positive slope in the emitted photon rate or, equivalently, that the emission of the first photon *on average* enhances the emission rate of the second. In previous work, we showed that the necessary criterion for a superradiant burst to be emitted from an initially fully excited ensemble of N two-level atoms is [48]

$$\mathrm{Var.}\left(\frac{\{\Gamma_\nu\}}{\Gamma_0}\right) \equiv \frac{1}{N}\sum_{\nu=1}^{N}\left(\frac{\Gamma_\nu^2}{\Gamma_0^2} - 1\right) > 1. \tag{8}$$

This condition assumes that all emitted light is collected. If that is not the case, one instead has to consider the rate of emission into the optical modes that are detected. A superradiant burst meeting certain criteria requires that the emission of the first photon on average enhances the rate of photons that meet those criteria. Further detail on these derived bounds are given in Appendix A.

2. Decay to multiple ground states

If there are multiple ground states, a superradiant burst is emitted by the fully excited state during decay to $|g_a\rangle$ if

$$\mathrm{Var.}\left(\frac{\{\Gamma^a_\nu\}}{\Gamma^a_0}\right) > \frac{\Gamma_0}{\Gamma^a_0}, \tag{9}$$

where $\Gamma_0 = \sum_a \Gamma^a_0$ is the total decay from the excited state. This is of the same form as Eq. (8), but the enhancement provided by the operators on the particular channel needs to additionally overcome competition between different "internal" channels. If all atoms are at a point, then the condition for a superradiant burst on a particular transition reduces to $\Gamma^a_0/\Gamma_0 > 1/(N-1)$.

3. Directional decay

In experiments, light is typically only collected in a particular direction. Directional superradiance is defined as the rate of photon emission into a particular direction having a positive slope, and can persist to much larger interatomic separations than when the entire emitted field is considered [50]. As shown in Appendix A, directional superradiance occurs if

$$\sum_{j,l=1}^{N} \mathrm{e}^{\mathrm{i}k^a_0 \mathbf{R}(\theta,\varphi)\cdot(\mathbf{r}_l - \mathbf{r}_j)} \frac{\Gamma^a_{jl}}{N\Gamma^a_0} > 1 + \frac{\Gamma_0}{\Gamma^a_0}, . \tag{10}$$

Here we map directional photon detection to atomic emission where $\mathbf{R}(\theta,\varphi)$ is a unit vector in the direction of the detector and $k^a_0 = 2\pi/\lambda^a_0$ the wavevector of the transition [18, 93]. We define the quantity

$$S = \frac{\sum_{j,l=1}^{N} \mathrm{e}^{\mathrm{i}k^a_0 \mathbf{R}(\theta,\varphi)\cdot(\mathbf{r}_l - \mathbf{r}_j)}\Gamma^a_{jl}}{N\left(\Gamma^a_0 + \Gamma_0\right)}, \tag{11}$$

such that if $S < 1$ the photon emission rate will decay monotonically in time, and if $S > 1$, the minimal conditions for superradiance are met.

C. Master equation evolution by cumulant expansion

It would be ideal to calculate the full dynamics to verify our predictions. However, the full Hilbert space scales exponentially with atom number. We approximate the full dynamics by means of a second-order cumulant expansion [94–96]. This method involves truncating the hierarchy of operator expectation values such that

$$\langle \hat{u}\hat{v}\hat{w}\rangle = \langle \hat{u}\hat{v}\rangle\langle \hat{w}\rangle + \langle \hat{v}\hat{w}\rangle\langle \hat{u}\rangle + \langle \hat{u}\hat{w}\rangle\langle \hat{v}\rangle - 2\langle \hat{u}\rangle\langle \hat{v}\rangle\langle \hat{w}\rangle . \tag{12}$$

The complexity of this expansion scales as $\mathcal{O}(N^3)$ rather than exponentially. Further details are provided in Appendix B. The accuracy of this approximation is not well-characterized for 2D arrays. We benchmark the method in Appendix C, showing that generically the accuracy is better for larger lattice constants.

V. SUPERRADIANCE IN 2D ARRAYS OF ALKALINE-EARTH ATOMS

We now consider AEA arrays where atoms are initialized in either one of the ${}^3\mathrm{D}_1\,|J=1,m_J=0\rangle$ or ${}^3\mathrm{D}_3\,|J=3,m_J=\{0,3\}\rangle$ states and allowed to decay [see Fig. 4]. Large inversion can be achieved with a short intense pulse of duration $\tau \ll (N\Gamma_0)^{-1}$ to prevent collective effects [97].

Decay from ${}^3\mathrm{D}_1\,|J=1,m_J=0\rangle$ can be simplified using information from Tables I and II. First, decay to ${}^3\mathrm{P}_2$ has minimal impact on the dynamics due to the reduced linewidth. Second, the subsequent decay from ${}^3\mathrm{P}_1 \rightarrow {}^1\mathrm{S}_0$ will not impact the initial burst as the decay is not fast enough, nor, due to the short wavelength, will it be strongly collectively enhanced. This leads to a four-level system, as shown in Fig. 4(a), with a bright linearly-polarized decay channel ${}^3\mathrm{D}_1\,|J=1,m_J=0\rangle \rightarrow {}^3\mathrm{P}_0\,|J=0,m_J=0\rangle$ and two dimmer circularly polarized transitions ${}^3\mathrm{D}_1\,|J=1,m_J=0\rangle \rightarrow {}^3\mathrm{P}_1\,|J=1,m_J=\pm1\rangle$. Note that the Clebsch-Gordan coefficient is zero for the ${}^3\mathrm{D}_1\,|J=1,m_J=0\rangle \rightarrow {}^3\mathrm{P}_1\,|J=1,m_J=0\rangle$ pathway. For simplicity, we treat decay to ${}^3\mathrm{P}_1\,|J=1,m_J=\pm1\rangle$ as split by large enough Zeeman shifts that photons on each transition are not seen by the other, but not by enough to significantly alter the wavelength of the transitions. Without such Zeeman shifts, photons of one circular polarization can drive transitions with the other, allowing the atoms to explore the full Zeeman structure and adding far greater complexity to the problem [98]. Similar structure of three decay channels would be obtained for initialization in ${}^3\mathrm{D}_1\,|J=1,m_J=\pm1\rangle$, but here the brightest transition is circularly-polarized which is generically less favorable than linearly-polarized transitions for superradiance [49].

We also consider atoms initialized in the ${}^3\mathrm{D}_3\,|J=3,m_J=0\rangle$ state. From here, there are also three decay channels, as shown in Fig. 4(b). As before, one is linearly polarized, that to ${}^3\mathrm{P}_2\,|J=2,m_J=0\rangle$, and the two decay channels to ${}^3\mathrm{P}_2\,|J=2,m_J=\pm1\rangle$ are circularly polarized. As above, we assume that these channels are independent due to sufficiently large Zeeman shifts. Alternatively, atoms initialized in ${}^3\mathrm{D}_3\,|J=3,m_J=3\rangle$ are effective two-level systems with circularly polarized decay, as the only decay channel is to ${}^3\mathrm{P}_2\,|J=2,m_J=2\rangle$. To study this situation, we rotate the magnetic field such that the dipole moment of the two-level systems is oriented as $\wp = \sqrt{1/2}\,(\hat{y}+\mathrm{i}\hat{z})$, so that the detector position is still perpendicular to the polarization axis, enhancing the signal. Other three (and two) decay channel systems could also be obtained by starting in different Zeeman levels in the ${}^3\mathrm{D}_3$ line.

We thus reduce the level structure of both atomic species to those shown in Fig. 4. Starting from states with $m_J = 0$, the master equation in Eq. (4) reduces to

$$\dot{\rho} = -\frac{\mathrm{i}}{\hbar}[\mathscr{H}_f+\mathscr{H}_g+\mathscr{H}_h,\rho]+\mathscr{L}_f(\rho)+\mathscr{L}_g(\rho)+\mathscr{L}_h(\rho), \tag{13}$$

where $|e\rangle$ is the excited state and $|f,g,h\rangle$ are the three ground states. For the two-level system we instead have

$$\dot{\rho} = -\frac{\mathrm{i}}{\hbar}[\mathscr{H}_g,\rho]+\mathscr{L}_g(\rho). \tag{14}$$

A. Many-body decay vs distance

We first investigate atoms initialized in the ${}^3\mathrm{D}_1\,|J=1,m_J=0\rangle$ state. We consider the condition given in Eq. (10) for the specific case of a square array of 12×12 atoms. The detector is placed along the x-axis, which should see significant emission as it is perpendicular to the dipole moment. For ^{174}Yb atoms, this detector would measure a superradiant burst on the

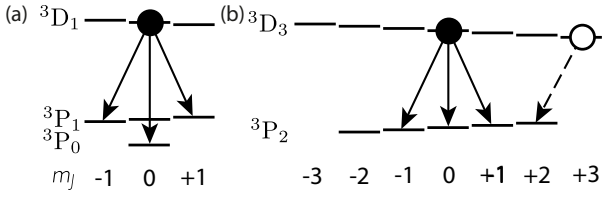

FIG. 4. Considered level structures. Atoms are initialized in the (a) ${}^3\mathrm{D}_1\,|J=1,m_J=0\rangle$ or (b) ${}^3\mathrm{D}_3\,|J=3,m_J=0,3\rangle$ state. In both $m_J=0$ cases, the internal structure is simplified into a toy model with three decay channels: a dominant linear π-polarized channel and two circularly polarized channels. In (a), the ${}^3\mathrm{P}_1\,|J=1,m_J=0\rangle$ state is not considered as the transition is forbidden.

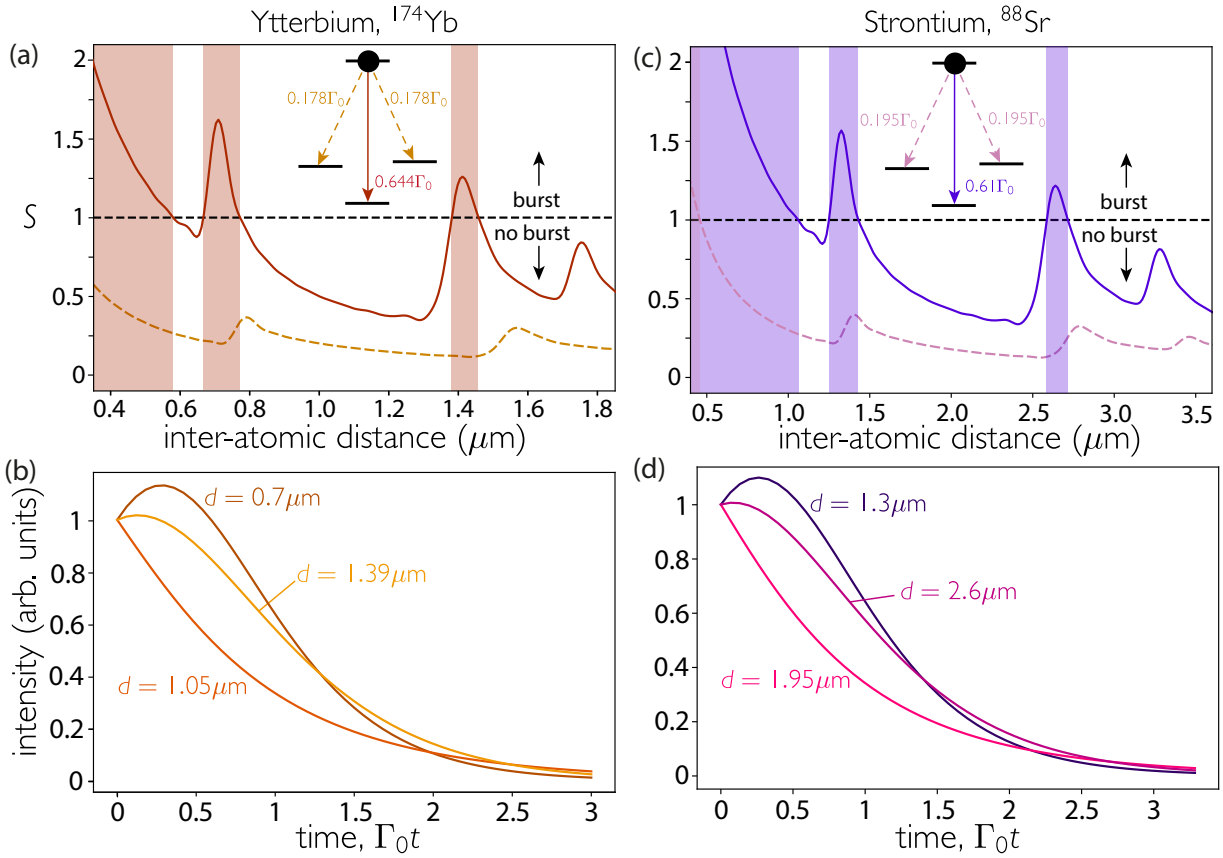

FIG. 5. Predictions of a burst versus lattice constant in 12×12 arrays of (a,b) ^{174}Yb and (c,d) ^{88}Sr. The atoms are prepared in the $^3\mathrm{D}_1\,|J = 1, m_J = 0\rangle$ state initially and allowed to decay, with the linear transition polarized perpendicular to the array. Light is detected along the x-axis. (a,c) The shaded areas indicate a burst on the $^3\mathrm{D}_1\,|J = 1, m_J = 0\rangle \rightarrow {}^3\mathrm{P}_0\,|J = 0, m_J = 0\rangle$ transition (red line), as the quantity S in Eq. (11) is larger than 1 (black dashed line). The $^3\mathrm{P}_1\,|J = 1, m_J = \pm 1\rangle$ transition (orange dashed line) is never superradiant. (b,d) Approximations of the full dynamics via a second-order cumulant expansion (on the $^3\mathrm{D}_1 \rightarrow {}^3\mathrm{P}_0$ transition) at three particular distances. As predicted by the superradiance condition, as the distance increases, the superradiant burst disappears and then reappears.

dominant transition for any interatomic separation satisfying $d < 0.6\,\mu$m, as shown in Fig. 5(a). This distance would be challenging for tweezer array experiments, but is achievable in an optical lattice [16, 17].

Superradiance can also be observed at particular "islands" where the set of decay operators combines to realize a sudden revival in emission in a particular direction. For this detector position, this occurs in regions centred on $d = 0.7\,\mu$m and $d = 1.4\,\mu$m, corresponding to a half and full wavelength of the brightest transition respectively. These revivals are due to geometric resonances where a mode that emits in this direction suddenly increases in amplitude due to Umklapp scattering, and thus becomes significantly brighter [99, 100]. While these processes can also revive global superradiance [48, 49], the effect is much more pronounced for directional superradiance [50]. This type of superradiance is highly dependent on the detector position, so the predicted distances change as a function of detector angle. The approximated full dynamics (via second-order cumulant expansion) agrees with our predictions, as shown in Fig. 5(b).

Superradiance can also be observed in ^{88}Sr. The dominant decay channel from $^3\mathrm{D}_1\,|J = 1, m_J = 0\rangle$ has a smaller branching ratio than that in ^{174}Yb, but due to its much longer wavelength, the constraints on interatomic distance are less tight. Figure 5(c) shows that a superradiant burst is always observed for $d < 1\,\mu$m. In addition, superradiance could be observed at the revivals with interatomic spacing $1.3\,\mu$m and $2.6\,\mu$m. Therefore, as in ^{174}Yb, as the interatomic spacing is increased, directional superradiance disappears and reappears. Strontium thus also offers a suitable platform for the direct observation of Dicke superradiance, despite the less favorable branching ratios to each state (see Tables I and II).

B. Collective "closing" of the atomic transition

Once a transition starts decaying superradiantly, it proceeds quickly, "stealing" photons from the other tran-

sition (as was discussed for the toy model described in Sec. III). The effect is stronger for smaller interatomic distances, because the superradiant burst is much faster in that regime. In Fig. 6, we plot the total photon share scattered on the dominant transition during superradiance. For ^{88}Sr, starting in the $^3\mathrm{D}_3\,|J=3,m_J=0\rangle$ state, a single atom scatters 60% of light on its brightest transition. By contrast, a 12×12 array overcomes the Clebsch-Gordan coefficient and scatters almost 70% on that transition. We see a similar improvement at telecom wavelengths for ^{174}Yb initialized in $^3\mathrm{D}_1\,|J=1,m_J=0\rangle$. As for the idealized case of atoms at a point, the light share increases logarithmically with atom number.

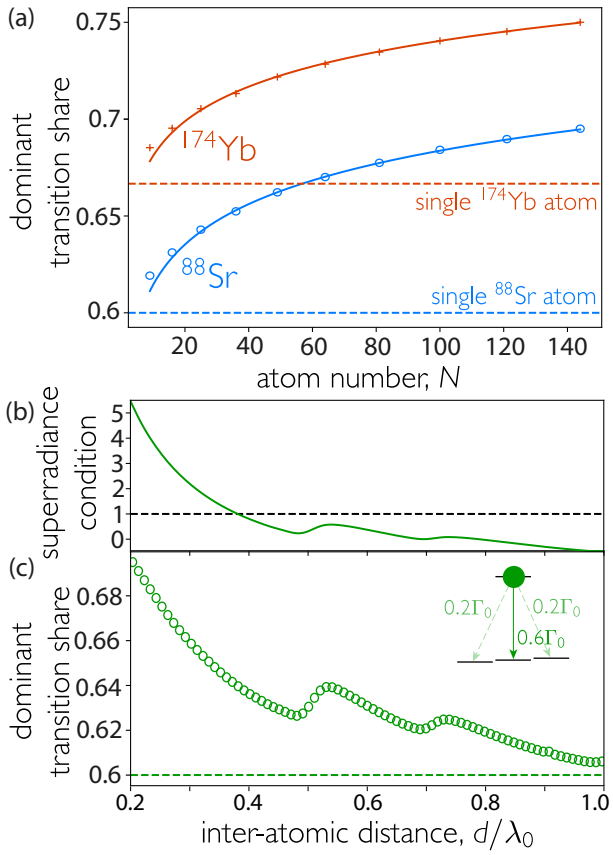

FIG. 6. Manipulation of branching ratios by collective emission. (a) Scaling of total share of light emitted on the brightest linearly-polarized transition (polarized perpendicular to the array) with atom number for square arrays of spacing $d=0.2\lambda_0$, obtained by second-order cumulant expansion simulations. Simulations for ^{174}Yb (^{88}Sr) are plotted in red (blue), with atoms initialized in the $^3\mathrm{D}_1\,|J=1,m_J=0\rangle$ ($^3\mathrm{D}_3\,|J=3,m_J=0\rangle$) state. Horizontal dashed lines represent the branching ratio for independent atoms. Solid lines are best fits to data from $N\geq25$ of the form $A\ln(N)+B$. For ^{174}Yb (^{88}Sr), the fit is $0.026\ln(N)+0.622$ ($0.030\ln(N)+0.545$). (b,c) 12×12 atoms are initialized in the $^3\mathrm{D}_3\,|J=3,m_J=0\rangle$ state. (b) The condition given by Eq. (9) in the form Var. $\left(\{\Gamma_\nu^{cd}\}/\Gamma_0^{cd}\right)-\Gamma_0/\Gamma_0^{cd}+1$; a global superradiant burst will be measured on the transition to $^3\mathrm{P}_2\,|J=2,m_J=0\rangle$ where the solid line is above the dashed line. (c) Total share of light emitted on the brightest linearly-polarized transition as the interatomic distance is changed.

The geometry of the array dictates the relative scattering on each channel and how much one can go beyond the ratio dictated by the single-atom Clebsch-Gordan coefficients. As the interatomic distance is increased, generally the transition is reopened, as shown in Fig. 6(c). However, revivals due to the geometric resonances can be seen by comparison to the variance of the set of decay rates [see Fig. 6(b)]. The revivals appear relatively minor but are capable of strongly impacting the decay dynamics. It should be noted that the condition for global superradiance is not met in the arrays of larger lattice constants, yet the closing of these weaker channels still occurs despite the fact that the avalanche is relatively weak.

The share could be further increased by intentionally seeding the transition with a small fraction of the atoms deterministically placed in the desired ground state, or an incomplete initial excitation from a particular ground state. Instead of relying on a quantum fluctuation to drive the start of the superradiant burst, these atoms would provide an artificial fluctuation. This would accelerate the superradiant burst on that seeded transition and generate a large atomic population in that state [30, 101, 102]. Nevertheless, how effectively this fluctuation will trigger the avalanche depends on its specific spatial profile and phase. We will thus not explore this avenue here.

C. Scaling of the burst

The largest possible burst occurs for atoms initialized in the $^3\mathrm{D}_3\,|J=3\rangle$ manifold. The transition wavelength is $\lambda_0=1.80$ μm for ^{174}Yb and $\lambda_0=2.92$ μm in ^{88}Sr. To minimize the interatomic distance, both species are assumed to be trapped in an optical lattice with 244 nm lattice spacing, corresponding to a wavelength of 488 nm for which Yb and Sr are trapped in the relevant states and high power lasers are available. This yields an interatomic spacing of $d=0.136\lambda_0$ for ^{174}Yb and $d=0.084\lambda_0$ for ^{88}Sr. We consider two initial states: $|J=3,m_J=0\rangle$ and $|J=3,m_J=3\rangle$. In the former case, decay is to three states, with a dominant transition that is linearly polarized. In the latter case, the atoms become effective two-level systems, decaying by circular σ^+-polarized light. This closed two-level transition can be accessed in all AEAs, including fermionic isotopes.

The largest possible burst is emitted by the simplest system operating at the longest wavelength, as shown in Fig. 7. For the effective two-level system, the peak intensity is more than three times greater than the initial intensity emitted by an array of 12×12 ^{174}Yb atoms, and more than six times greater for ^{88}Sr. The peak scales as $\sim N^{1.38}$ and $\sim N^{1.47}$ for ^{174}Yb and ^{88}Sr respectively. The smaller peak emitted from the $|J=3,m_J=0\rangle$ state is still significant, and scales as $\sim N^{1.29}$ for ^{174}Yb and

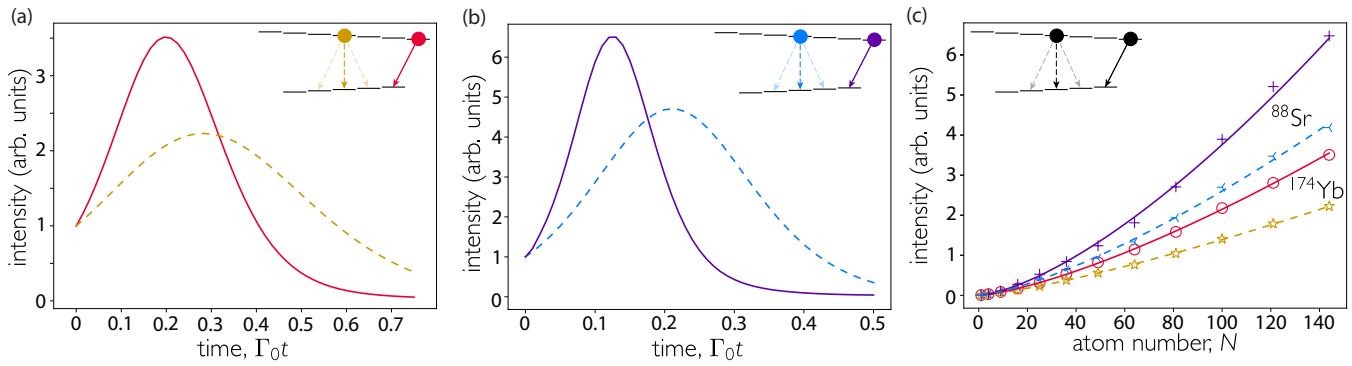

FIG. 7. Largest superradiant burst in ordered 2D arrays of AEAs. (a) ^{174}Yb and (b) ^{88}Sr atoms are initialized in $^3\mathrm{D}_3\,|J=3,m_J=0\rangle$, with the dominant linear transition polarized perpendicular to the array, or $^3\mathrm{D}_3\,|J=3,m_J=3\rangle$, with the only possible decay having $\sqrt{1/2}\,(\hat{y}+\mathrm{i}\hat{z})$ polarization. Second-order cumulant expansion simulations of the superradiant burst emitted on the (dashed) $^3\mathrm{D}_3\,|J=3,m_J=0\rangle \rightarrow ^3\mathrm{P}_2\,|J=2,m_J=0\rangle$, with parasitic decays to $|J=2,m_J=\pm1\rangle$, and (solid) $^3\mathrm{D}_3\,|J=3,m_J=3\rangle \rightarrow ^3\mathrm{P}_2\,|J=2,m_J=2\rangle$ transition. (c) Scaling of the peak intensity with atom number. Lines are power law fits of data with $N \geq 25$. For the effective two-level system, the scaling of the peak is $N^{1.38}$ for ^{174}Yb and $N^{1.47}$, while the four-level system scales as $N^{1.29}$ for ^{174}Yb and $N^{1.37}$ for ^{88}Sr. In all plots, the lattice constant is $d = 244\,\mathrm{nm}$.

$\sim N^{1.37}$ for ^{88}Sr. A word of caution is needed though, as the validity of the second-order cumulant expansion is not well characterized for these large atom numbers at such small distances, and may overestimate the burst due to significant multipartite correlations [96].

VI. CONCLUSIONS

We have presented results on collective decay in realistic arrays of alkaline earth atoms. Building on previous work, we calculate conditional correlation functions to predict the nature of the collective decay. We predict highly non-trivial many-body decay through control of the interatomic spacing of the array and position of the detector. Focussing on the particular cases of ^{88}Sr and ^{174}Yb, we show that the observation of Dicke superradiance should be feasible in such systems. Furthermore, we show that by increasing the interatomic separation, Dicke superradiance is attenuated and lost, but is then revived at a larger distance. We show that this understanding can be used to manipulate how much population ends up in each possible ground state.

Experiments are critical to understand many-body decay, as full dynamics are only obtained via approximations. We have focused on strontium and ytterbium due to the recent progress in implementing atomic arrays with these species, and the favorable set of transitions to achieve subwavelength interatomic spacing. However, similar results should also be possible with other alkaline earth elements, which have the same structure, but where progress in cooling and trapping is less advanced [103–106]. The relative spacing (and order) of levels is different in all these atoms. For example, in radium, there is a two-level linearly-polarized transition - as the $^3\mathrm{D}_1$ state can only decay to $^3\mathrm{P}_0$ - at a far-infrared wavelength of $\sim 16\,\mu$m [107]. Rare earth elements also have infrared transitions from the ground state, and can be similarly trapped in short wavelengths due to strong blue transitions [108–111].

Our results may be relevant in the context of Rydberg quantum simulators [112–114]. Excited Rydberg states can decay via a fast short-wavelength transition (and therefore not collectively enhanced) or via much slower but very long-wavelength transitions. Our work implies that the amount of light scattered on these long Rydberg-Rydberg transitions could be significantly enhanced by collective decay [89, 115, 116]. Furthermore, understanding the collective enhancement of coupling between black body photons and the $^3\mathrm{P}_0$ state in atomic optical lattice clocks is key to achieving high precision in compact devices [117–119].

The control of the atoms is translated into control over the emitted light. For example, initial superposition states will emit superpositions of different pulses, with the potential for generation of macroscopic superposition states of light. In particular, the potential for ^{174}Yb arrays to produce non-classical light at telecom frequencies is tantalizing. While we have focused on the interatomic spacing of the array and the relative position of the detector to control the decay, there are additional tuning knobs that could be harnessed. The dynamics, and in particular the directionality, could be altered by changing the geometry of the array, either by modifying the lattice or the global shape. Manipulation of the initial state, adding coherent or incoherent drives, or manual addition of site-specific inhomogeneity [120]; all of this will impact the dynamics and steady state of the system.

Understanding the various decay processes - and freezing out coherent dynamics - opens up possibilities to harness them. For instance, the complex dissipative dynamics provides a method to access highly entangled

dark states that completely decouple from the environment. The deterministic production of these states, and their potential as resources for quantum computing and metrology [121, 122], remains an exciting open problem.

VII. ACKNOWLEDGEMENTS

We are grateful to Francis Robicheaux, Oriol Rubies-Bigorda, Silvia Cardenas-Lopez, Debayan Mitra and Hannes Bernien for useful discussions. A.A.-G. acknowledges support by the National Science Foundation through the CAREER Award (No. 2047380) and the QII-TAQS program (Award No. 1936359), the Air Force Office of Scientific Research through their Young Investigator Prize (grant No. 21RT0751), as well as by the A. P. Sloan Foundation. A.A.-G. also acknowledges the Flatiron Institute, where some of this work was performed. A.A.-G. and S.J.M. acknowledge additional support by the David and Lucile Packard Foundation. J.P.C. acknowledges support from the NSF PHY Division (Award No. 2112663). S.W. acknowledges support by the National Science Foundation through the QII-TAQS program (Award No. 1936359) and the Alfred P. Sloan Foundation. We acknowledge computing resources from Columbia University's Shared Research Computing Facility project, which is supported by NIH Research Facility Improvement Grant 1G20RR030893-01, and associated funds from the New York State Empire State Development, Division of Science Technology and Innovation (NYSTAR) Contract C090171, both awarded April 15, 2010.

APPENDIX A: DERIVATION OF DIRECTIONAL CONDITION FOR SUPERRADIANCE ON A PARTICULAR CHANNEL

The dissipator of Eq. (6) can be expressed in terms of a set of collective lowering operators $\{\hat{\mathbb{O}}_{\nu,a}\}$. These are generically superpositions of the form

$$\hat{\mathbb{O}}_{\nu,a} = \sum_{j=1}^{N} \alpha_{\nu,a,j} \hat{\sigma}^{j}_{g_a e}. \tag{15}$$

The coefficients $\alpha_{\nu,a,j}$ are found as the eigenstates of the dissipative interaction matrix $\mathbf{\Gamma}^a$ with elements Γ^a_{jl}, with their rates, $\{\Gamma^a_\nu\}$, given by the corresponding eigenvalues. Each Lindbladian term is thus recast as

$$\mathcal{L}_a(\rho) = \sum_{\nu=1}^{N} \frac{\Gamma^a_\nu}{2} \left(2\hat{\mathbb{O}}_{\nu,a}\rho\,\hat{\mathbb{O}}^\dagger_{\nu,a} - \hat{\mathbb{O}}^\dagger_{\nu,a}\hat{\mathbb{O}}_{\nu,a}\rho - \rho\,\hat{\mathbb{O}}^\dagger_{\nu,a}\hat{\mathbb{O}}_{\nu,a} \right). \tag{16}$$

Dissipation can thus be understood as the emission of a photon into one of the N possible decay channels.

Appendix A.1: Multiple ground states

The derivative of the intensity emitted on a specified transition $|e\rangle \to |g_a\rangle$ is positive if

$$\frac{\sum_{\mu=1}^{N} \sum_{b} \sum_{\nu=1}^{N} \langle \hat{\mathbb{O}}^\dagger_{\nu,b} \hat{\mathbb{O}}^\dagger_{\mu,a} \hat{\mathbb{O}}_{\mu,a} \hat{\mathbb{O}}_{\nu,b} \rangle}{\left(\sum_{b} \sum_{\nu=1}^{N} \langle \hat{\mathbb{O}}^\dagger_{\nu,b} \hat{\mathbb{O}}_{\nu,b} \rangle \right) \left(\sum_{\mu=1} \langle \hat{\mathbb{O}}^\dagger_{\mu,a} \hat{\mathbb{O}}_{\mu,a} \rangle \right)} > 1, \tag{17}$$

On a fully excited initial state, this expression reads

$$1 + \frac{\sum_{\nu=1}^{N} (\Gamma^a_v)^2}{N^2 \Gamma^a_0 \Gamma_0} - \frac{1}{N} - \frac{\Gamma^a_0}{N\Gamma_0} > 1, \tag{18}$$

which simplifies to

$$\text{Var.}\left(\frac{\Gamma^a_\nu}{\Gamma^a_0}\right) \equiv \frac{1}{N} \sum_{\nu=1}^{N} \left[\left(\frac{\Gamma^a_\nu}{\Gamma^a_0} \right)^2 - 1 \right] > \frac{\Gamma_0}{\Gamma^a_0} \tag{19}$$

where $\Gamma_0 = \sum_a \Gamma^a_0$ is the total excited state decay rate.

Appendix A.2: Directional decay

Detection of a photon from a given transition in far-field in a direction governed by spherical angles $\{\theta, \varphi\}$ can be mapped to the collective lowering operator [18, 93]

$$\hat{\mathbb{D}}_a(\theta,\varphi) = \sqrt{\frac{3\Gamma^a_0}{8\pi} \left[1 - (\boldsymbol{\wp}_a \cdot \mathbf{R}(\theta,\varphi))^2 \right] \mathrm{d}\Omega} \times \sum_{j=1}^{N} \mathrm{e}^{-\mathrm{i}k^a_0 \mathbf{R}(\theta,\varphi)\cdot \mathbf{r}_j} \hat{\sigma}^j_{g_a e}, \tag{20}$$

where $\mathbf{R}(\theta,\varphi)$ is a unit vector in the direction of the detector, $\mathrm{d}\Omega$ is a solid angle increment and k^a_0 is the wavevector of the transition. Using these, the derivative of the intensity emitted on a specified transition $|e\rangle \to |g_a\rangle$ in a direction $\{\theta,\varphi\}$ is positive if

$$\frac{\sum_{b} \sum_{\nu=1}^{N} \langle \hat{\mathbb{O}}^\dagger_{\nu,b} \hat{\mathbb{D}}^\dagger_a(\theta,\varphi) \hat{\mathbb{D}}_a(\theta,\varphi) \hat{\mathbb{O}}_{\nu,b} \rangle}{\sum_{b} \left(\sum_{\nu=1}^{N} \langle \hat{\mathbb{O}}^\dagger_{\nu,b} \hat{\mathbb{O}}_{\nu,b} \rangle \right) \langle \hat{\mathbb{D}}^\dagger_a(\theta,\varphi) \hat{\mathbb{D}}_a(\theta,\varphi) \rangle} > 1. \tag{21}$$

On a fully excited state, this expression reads,

$$1 + \frac{\sum_{j,l=1}^{N} \mathrm{e}^{\mathrm{i}k_0 \mathbf{R}(\theta,\varphi)\cdot(\mathbf{r}_l - \mathbf{r}_j)} \Gamma_{jl}}{N^2 \Gamma_0} - \frac{1}{N} - \frac{\Gamma^a_0}{N\Gamma_0} > 1 \tag{22}$$

where we have employed that

$$\sum_{\nu=1}^{N} \Gamma^a_v \alpha^*_{\nu,a,j} \alpha_{\nu,a,l} = \Gamma^a_{jl}. \tag{23}$$

This simplifies to

$$\sum_{j,l=1}^{N} \mathrm{e}^{\mathrm{i}k_0^a \mathbf{R}(\theta,\varphi)(\mathbf{r}_l-\mathbf{r}_j)} \frac{\Gamma_{jl}^a}{N\Gamma_0^a} > 1 + \frac{\Gamma_0}{\Gamma_0^a}. \tag{24}$$

APPENDIX B: SECOND-ORDER CUMULANT EXPANSION FOR FOUR-LEVEL SYSTEMS

We consider four-level atoms that can decay to three ground states $|f,g,h\rangle$ from an excited state $|e\rangle$. Photons associated to each transition $|e\rangle \to |f,g,h\rangle$ are sufficiently distinct in frequency to not excite one another. To calculate the directional intensity on a channel $|e\rangle \to |f\rangle$, we require the evolution of the expectation values of the set $\{\hat{\sigma}_{ef}^i \hat{\sigma}_{fe}^j\}$, requiring at least a second-order cumulant expansion. Generically, the evolution of these expectation values depends on the expectation values of sets of three of the population operators, e.g. $\{\hat{\sigma}_{ee}^i\}$ (the fourth can be related to the other three as the total single atom population is always unity), all six coherence operators, e.g., $\{\hat{\sigma}_{ef}^i\}$, and all 66 two-operator products, noting that the complex expectation value of the coherence operators leads to extra operators such as $\{\hat{\sigma}_{ef}^i \hat{\sigma}_{fe}^j\}$.

If the initial state has no coherence, such that initially

$$\{\langle \hat{\sigma}_{ab}^i \rangle\} = 0 \; \forall \; a,b \;\text{ and }\; \{\langle \hat{\sigma}_{ab}^i \hat{\sigma}_{cd}^j \rangle\} = 0 \; \forall \; a,b,c,d, \tag{25}$$

then the equations are greatly simplified. This condition is met by the fully excited state, or any state where all single atom states are the ground or excited state. In this case, the single atom coherences are never different from zero in the second-order cumulant expansion and the expectation values of all two-operator products of the form $\{\hat{\sigma}_{ab}^i \hat{\sigma}_{ad}^j\}$ are always zero, and those of the form $\hat{\sigma}_{ab}^i \hat{\sigma}_{da}^j$ are zero $\forall\, b \neq d$. The two-operator products of the form $\{\hat{\sigma}_{aa}^i \hat{\sigma}_{bb}^j\}$ and $\{\hat{\sigma}_{ab}^i \hat{\sigma}_{ba}^j\}$ do become non-zero, but only those where one of a or b represents the excited state impact the evolution of the terms needed to calculate directional intensity. As such, there is a closed set of operators with expectation values defined as

$$a_j = \langle \hat{\sigma}_{ee}^j \rangle, b_j = \langle \hat{\sigma}_{ff}^j \rangle, c_j = \langle \hat{\sigma}_{gg}^j \rangle, \tag{26a}$$

$$e_{jl} = \langle \hat{\sigma}_{ee}^j \hat{\sigma}_{ee}^l \rangle, f_{jl} = \langle \hat{\sigma}_{ee}^j \hat{\sigma}_{ff}^l \rangle, g_{jl} = \langle \hat{\sigma}_{ee}^j \hat{\sigma}_{gg}^l \rangle, \tag{26b}$$

$$q_{jl} = \langle \hat{\sigma}_{ef}^j \hat{\sigma}_{fe}^l \rangle, p_{jl} = \langle \hat{\sigma}_{eg}^j \hat{\sigma}_{ge}^l \rangle, r_{jl} = \langle \hat{\sigma}_{eh}^j \hat{\sigma}_{he}^l \rangle. \tag{26c}$$

The expectation values evolve according to

$$\dot{a}_j = -\Gamma_0 a_j + \mathrm{i} \sum_{m=1}^{N} \left[-A_{jm} q_{jm} + A_{jm}^* q_{mj} - B_{mj} p_{jm} + B_{mj}^* p_{mj} - C_{jm} r_{jm} + C_{mj}^* r_{mj} \right], \tag{27a}$$

$$\dot{b}_j = \Gamma_0^{ef} a_j + \mathrm{i} \sum_{m=1}^{N} \left[-A_{mj}^* q_{mj} + A_{jm} q_{jm} \right], \tag{27b}$$

$$\dot{c}_j = \Gamma_0^{eg} a_j + \mathrm{i} \sum_{m=1}^{N} \left[-B_{mj}^* p_{mj} + B_{jm} p_{jm} \right], \tag{27c}$$

$$\begin{aligned} \dot{e}_{jl} = {} & -2\Gamma_0 e_{jl} + \mathrm{i} \sum_l \Big[-A_{jm} \langle \hat{\sigma}_{ef}^j \hat{\sigma}_{ee}^l \hat{\sigma}_{fe}^m \rangle - A_{jm} \langle \hat{\sigma}_{ee}^j \hat{\sigma}_{ef}^l \hat{\sigma}_{fe}^m \rangle - B_{jm} \langle \hat{\sigma}_{eg}^j \hat{\sigma}_{ee}^l \hat{\sigma}_{ge}^m \rangle - B_{jm} \langle \hat{\sigma}_{ee}^j \hat{\sigma}_{eg}^l \hat{\sigma}_{ge}^m \rangle - C_{jm} \langle \hat{\sigma}_{eh}^j \hat{\sigma}_{ee}^l \hat{\sigma}_{he}^m \rangle \\ & - C_{jm} \langle \hat{\sigma}_{ee}^j \hat{\sigma}_{eh}^l \hat{\sigma}_{he}^m \rangle + A_{mj}^* \langle \hat{\sigma}_{fe}^j \hat{\sigma}_{ee}^l \hat{\sigma}_{ef}^m \rangle + A_{ml}^* \langle \hat{\sigma}_{ee}^j \hat{\sigma}_{fe}^l \hat{\sigma}_{ef}^m \rangle + B_{mj}^* \langle \hat{\sigma}_{ge}^j \hat{\sigma}_{ee}^l \hat{\sigma}_{eg}^m \rangle + B_{ml}^* \langle \hat{\sigma}_{ee}^j \hat{\sigma}_{ge}^l \hat{\sigma}_{eg}^m \rangle + C_{mj}^* \langle \hat{\sigma}_{he}^j \hat{\sigma}_{ee}^l \hat{\sigma}_{ef}^m \rangle \\ & + C_{ml}^* \langle \hat{\sigma}_{ee}^j \hat{\sigma}_{he}^l \hat{\sigma}_{ef}^m \rangle \Big], \end{aligned} \tag{27d}$$

$$\begin{aligned} \dot{f}_{jl} = {} & -\Gamma_0 f_{jl} - \mathrm{i} A_{jl} q_{jl} + \mathrm{i} A_{ji}^* q_{ji} + \Gamma_0^A e_{jl} + \mathrm{i} \sum_l \Big[-A_{jm} \langle \hat{\sigma}_{ef}^j \hat{\sigma}_{ff}^l \hat{\sigma}_{fe}^m \rangle - A_{ml}^* \langle \hat{\sigma}_{ee}^j \hat{\sigma}_{fe}^l \hat{\sigma}_{ef}^m \rangle - B_{jm} \langle \hat{\sigma}_{eg}^j \hat{\sigma}_{ff}^l \hat{\sigma}_{ge}^m \rangle \\ & - C_{jm} \langle \hat{\sigma}_{eh}^j \hat{\sigma}_{ff}^l \hat{\sigma}_{he}^m \rangle + A_{mj}^* \langle \hat{\sigma}_{fe}^j \hat{\sigma}_{ff}^l \hat{\sigma}_{ef}^m \rangle + A_{jm} \langle \hat{\sigma}_{ee}^j \hat{\sigma}_{ef}^l \hat{\sigma}_{fe}^m \rangle + B_{mj}^* \langle \hat{\sigma}_{ge}^j \hat{\sigma}_{ff}^l \hat{\sigma}_{eg}^m \rangle + C_{mj}^* \langle \hat{\sigma}_{he}^j \hat{\sigma}_{ff}^l \hat{\sigma}_{ef}^m \rangle \Big], \end{aligned} \tag{27e}$$

$$\begin{aligned} \dot{g}_{jl} = {} & -\Gamma_0 g_{jl} - \mathrm{i} B_{jl} p_{jl} + \mathrm{i} B_{ji}^* p_{ji} + \Gamma_0^B e_{jl} + \mathrm{i} \sum_l \Big[-B_{jm} \langle \hat{\sigma}_{eg}^j \hat{\sigma}_{gg}^l \hat{\sigma}_{ge}^m \rangle - B_{ml}^* \langle \hat{\sigma}_{ee}^j \hat{\sigma}_{ge}^l \hat{\sigma}_{eg}^m \rangle - A_{jm} \langle \hat{\sigma}_{ef}^j \hat{\sigma}_{gg}^l \hat{\sigma}_{fe}^m \rangle \\ & - C_{jm} \langle \hat{\sigma}_{eh}^j \hat{\sigma}_{gg}^l \hat{\sigma}_{he}^m \rangle + B_{mj}^* \langle \hat{\sigma}_{ge}^j \hat{\sigma}_{gg}^l \hat{\sigma}_{eg}^m \rangle + B_{jm} \langle \hat{\sigma}_{ee}^j \hat{\sigma}_{eg}^l \hat{\sigma}_{ge}^m \rangle + A_{mj}^* \langle \hat{\sigma}_{fe}^j \hat{\sigma}_{gg}^l \hat{\sigma}_{ef}^m \rangle + C_{mj}^* \langle \hat{\sigma}_{he}^j \hat{\sigma}_{gg}^l \hat{\sigma}_{ef}^m \rangle \Big], \end{aligned} \tag{27f}$$

$$\begin{aligned} \dot{q}_{jl} = {} & -\Gamma_0 q_{jl} - \mathrm{i} A_{ji} f_{jl} + \mathrm{i} A_{ji}^* f_{ji} + \Gamma_{ji}^A e_{jl} + \mathrm{i} \sum_l \Big[-A_{mj}^* \langle \hat{\sigma}_{ee}^j \hat{\sigma}_{fe}^l \hat{\sigma}_{ef}^m \rangle - A_{jm} \langle \hat{\sigma}_{ef}^j \hat{\sigma}_{ff}^l \hat{\sigma}_{fe}^m \rangle + A_{mj}^* \langle \hat{\sigma}_{ff}^j \hat{\sigma}_{fe}^l \hat{\sigma}_{ef}^m \rangle \\ & + A_{jm} \langle \hat{\sigma}_{ef}^j \hat{\sigma}_{ee}^l \hat{\sigma}_{fe}^m \rangle \Big], \end{aligned} \tag{27g}$$

$$\dot{p}_{jl} = -\Gamma_0 p_{jl} - \mathrm{i} B_{ji} g_{jl} + \mathrm{i} B_{ji}^* g_{ji} + \Gamma_{ji}^B e_{jl} + \mathrm{i} \sum_l \left[-B_{mj}^* \langle \hat{\sigma}_{ee}^j \hat{\sigma}_{ge}^l \hat{\sigma}_{eg}^m \rangle - B_{jm} \langle \hat{\sigma}_{eg}^j \hat{\sigma}_{gg}^l \hat{\sigma}_{ge}^m \rangle + B_{mj}^* \langle \hat{\sigma}_{gg}^j \hat{\sigma}_{ge}^l \hat{\sigma}_{eg}^m \rangle \right.$$

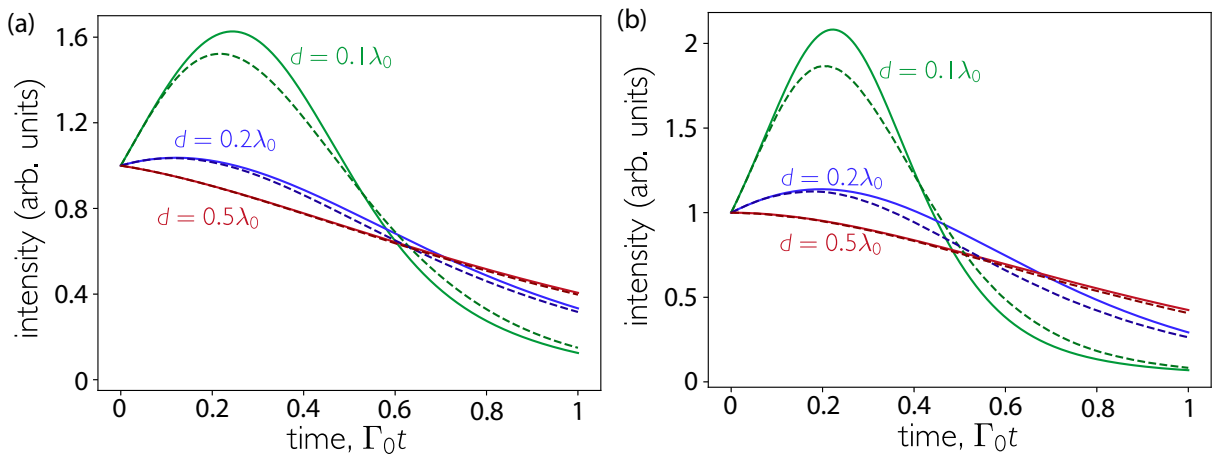

FIG. 8. Benchmarking of second-order cumulant expansion against exact dynamics. Light emitted by a (a) 3×3 and (b) 4×4 array of two-level systems prepared initially in the excited state with polarization axis perpendicular to the array. Light is detected along the x-axis. Cumulant expansion dynamics (solid lines) are compared to exact dynamics (dashed lines), which are obtained from the master equation in (a) and from an ensemble average of 10,000 quantum trajectories in (b).

$$+B_{jm}\left\langle\hat{\sigma}_{eg}^{j}\hat{\sigma}_{ee}^{l}\hat{\sigma}_{ge}^{m}\right\rangle\big]\,, \tag{27h}$$

$$\dot{r}_{jl} = -\Gamma_0 r_{jl} - \mathrm{i}C_{ji}\left(a_i - e_{jl} - f_{jl} - g_{jl}\right) + \mathrm{i}C_{ji}^{*}(a_j - e_{ji} - f_{ji} - g_{jl}) + \Gamma_{ji}^{C} e_{jl} + \mathrm{i}\sum_{l}\big[-C_{mj}^{*}\left\langle\hat{\sigma}_{ee}^{j}\hat{\sigma}_{he}^{l}\hat{\sigma}_{ef}^{m}\right\rangle$$

$$-C_{jm}\left\langle\hat{\sigma}_{eh}^{j}\hat{\sigma}_{hh}^{l}\hat{\sigma}_{he}^{m}\right\rangle + C_{mj}^{*}\left\langle\hat{\sigma}_{hh}^{j}\hat{\sigma}_{he}^{l}\hat{\sigma}_{ef}^{m}\right\rangle + C_{jm}\left\langle\hat{\sigma}_{eh}^{j}\hat{\sigma}_{ee}^{l}\hat{\sigma}_{he}^{m}\right\rangle\Big]\,, \tag{27i}$$

where we have defined that

$$A_{jl} = J_{jl}^{ef} - \mathrm{i}\frac{\Gamma_{jl}^{ef}}{2}, B_{jl} = J_{jl}^{eg} - \mathrm{i}\frac{\Gamma_{jl}^{eg}}{2}, C_{jl} = J_{jl}^{eh} - \mathrm{i}\frac{\Gamma_{jl}^{eh}}{2}, \tag{28}$$

and three-operator product expectation values are approximated by the second-order cumulant expansion as

$$\langle\hat{u}\hat{v}\hat{w}\rangle = \langle\hat{u}\hat{v}\rangle\langle\hat{w}\rangle + \langle\hat{v}\hat{w}\rangle\langle\hat{u}\rangle + \langle\hat{u}\hat{w}\rangle\langle\hat{v}\rangle - 2\langle\hat{u}\rangle\langle\hat{v}\rangle\langle\hat{w}\rangle\,. \tag{29}$$

APPENDIX C: BENCHMARKING SECOND-ORDER CUMULANT EXPANSION

To benchmark the second-order cumulant expansion we compare the approximated dynamics to the exact dynamics for small system sizes, as shown in Fig. 8. Here, we consider two-level atoms as calculating exact dynamics for four-level atoms is not computationally tractable for even 16 atoms. Exact dynamics are found as the ensemble average of quantum trajectories [123]. At short times, and for modest separations, the cumulant expansion is an excellent approximation of the dynamics. As the distance decreases, the error becomes more significant. For $d = 0.1\lambda_0$, the peak is overestimated by 12% for a 4×4 array, and by 9% for a 3×3 array. The relative error is much larger at later times as the cumulant expansion is unable to capture the subradiant tail [95]. This is also true for $d = 0.2\lambda_0$, where the burst is captured more accurately (overestimated by only 1% for a 4×4 array), but large relative errors occur in the tail.

[1] R. H. Dicke, Coherence in spontaneous radiation processes, Phys. Rev. **93**, 99 (1954).

[2] M. Gross and S. Haroche, Superradiance: An essay on the theory of collective spontaneous emission, Phys. Rep. **93**, 301 (1982).

[3] M. G. Benedict, A. M. Ermolaev, V. A. Malyshev, I. V. Sokolov, and E. D. Trifonov, *Super-radiance: Multiatomic Coherent Emission* (CRC Press, 1996).

[4] J. M. Raimond, P. Goy, M. Gross, C. Fabre, and S. Haroche, Collective absorption of blackbody radiation by Rydberg atoms in a cavity: An experiment on Bose statistics and Brownian motion, Phys. Rev. Lett. **49**, 117 (1982).

[5] S. Slama, S. Bux, G. Krenz, C. Zimmermann, and P. W. Courteille, Superradiant Rayleigh scattering and collective atomic recoil lasing in a ring cavity, Phys. Rev. Lett. **98**, 053603 (2007).

[6] S. Inouye, A. P. Chikkatur, D. M. Stamper-Kurn, J. Stenger, D. E. Pritchard, and W. Ketterle, Superradiant Rayleigh scattering from a Bose-Einstein condensate, Science **285**, 571 (1999).

[7] D. Schneble, Y. Torii, M. Boyd, E. W. Streed, D. E. Pritchard, and W. Ketterle, The onset of matter-wave amplification in a superradiant Bose-Einstein condensate, Science **300**, 475 (2003).

[8] Y. Yoshikawa, Y. Torii, and T. Kuga, Superradiant light scattering from thermal atomic vapors, Phys. Rev. Lett. **94**, 083602 (2005).

[9] D. Meiser, J. Ye, D. R. Carlson, and M. J. Holland, Prospects for a millihertz-linewidth laser, Phys. Rev. Lett. **102**, 163601 (2009).

[10] J. G. Bohnet, Z. Chen, J. M. Weiner, D. Meiser, M. J. Holland, and J. K. Thompson, A steady-state superradiant laser with less than one intracavity photon, Nature **484**, 78 (2012).

[11] K. Baumann, C. Guerlin, F. Brennecke, and T. Esslinger, Dicke quantum phase transition with a superfluid gas in an optical cavity, Nature **464**, 1301 (2010).

[12] Z. Zhang, C. H. Lee, R. Kumar, K. J. Arnold, S. J. Masson, A. L. Grimsmo, A. S. Parkins, and M. D. Barrett, Dicke-model simulation via cavity-assisted Raman transitions, Phys. Rev. A **97**, 043858 (2018).

[13] O. Hosten, N. J. Engelsen, R. Krishnakumar, and M. A. Kasevich, Measurement noise 100 times lower than the quantum-projection limit using entangled atoms, Nature **529**, 505 (2016).

[14] K. C. Cox, G. P. Greve, J. M. Weiner, and J. K. Thompson, Deterministic squeezed states with collective measurements and feedback, Phys. Rev. Lett. **116**, 093602 (2016).

[15] S. Colombo, E. Pedrozo-Peñafiel, A. F. Adiyatullin, Z. Li, E. Mendez, C. Shu, and V. Vuletić, Time-reversal-based quantum metrology with many-body entangled states, Nat. Phys. **18**, 925 (2022).

[16] J. Rui, D. Wei, A. Rubio-Abadal, S. Hollerith, J. Zeiher, D. M. Stamper-Kurn, C. Gross, and I. Bloch, A subradiant optical mirror formed by a single structured atomic layer, Nature **583**, 369 (2020).

[17] K. Srakaew, P. Weckesser, S. Hollerith, D. Wei, D. Adler, I. Bloch, and J. Zeiher, A subwavelength atomic array switched by a single Rydberg atom, Nat. Phys. 10.1038/s41567-023-01959-y (2023).

[18] J. P. Clemens, L. Horvath, B. C. Sanders, and H. J. Carmichael, Collective spontaneous emission from a line of atoms, Phys. Rev. A **68**, 023809 (2003).

[19] M. O. Scully, E. S. Fry, C. H. Raymond Ooi, and K. Wódkiewicz, Directed spontaneous emission from an extended ensemble of N atoms: Timing is everything, Phys. Rev. Lett. **96**, 010501 (2006).

[20] D. Bhatti, J. von Zanthier, and G. S. Agarwal, Superbunching and nonclassicality as new hallmarks of superradiance, Sci. Rep. **5**, 17335 (2015).

[21] Q.-u.-A. Gulfam and Z. Ficek, Highly directional photon superbunching from a few-atom chain of emitters, Phys. Rev. A **98**, 063824 (2018).

[22] I. Liberal, I. Ederra, and R. W. Ziolkowski, Grating lobes in higher-order correlation functions of arrays of quantum emitters: Directional photon bunching versus correlated directions, Photonics **6**, 14 (2019).

[23] R. Holzinger, M. Moreno-Cardoner, and H. Ritsch, Nanoscale continuous quantum light sources based on driven dipole emitter arrays, *Applied Physics Letters*, Appl. Phys. Lett. **119**, 024002 (2021).

[24] W. Guerin, M. O. Araújo, and R. Kaiser, Subradiance in a large cloud of cold atoms, Phys. Rev. Lett. **116**, 083601 (2016).

[25] P. Solano, P. Barberis-Blostein, F. K. Fatemi, L. A. Orozco, and S. L. Rolston, Super-radiance reveals infinite-range dipole interactions through a nanofiber, Nat. Commun. **8**, 1857 (2017).

[26] M. Hebenstreit, B. Kraus, L. Ostermann, and H. Ritsch, Subradiance via entanglement in atoms with several independent decay channels, Phys. Rev. Lett. **118**, 143602 (2017).

[27] S. J. Masson, I. Ferrier-Barbut, L. A. Orozco, A. Browaeys, and A. Asenjo-Garcia, Many-body signatures of collective decay in atomic chains, Phys. Rev. Lett. **125**, 263601 (2020).

[28] A. Cipris, N. A. Moreira, T. S. do Espirito Santo, P. Weiss, C. J. Villas-Boas, R. Kaiser, W. Guerin, and R. Bachelard, Subradiance with saturated atoms: Population enhancement of the long-lived states, Phys. Rev. Lett. **126**, 103604 (2021).

[29] G. Ferioli, A. Glicenstein, L. Henriet, I. Ferrier-Barbut, and A. Browaeys, Storage and release of subradiant excitations in a dense atomic cloud, Phys. Rev. X **11**, 021031 (2021).

[30] A. Piñeiro Orioli, J. K. Thompson, and A. M. Rey, Emergent dark states from superradiant dynamics in multilevel atoms in a cavity, Phys. Rev. X **12**, 011054 (2022).

[31] A. C. Santos, A. Cidrim, C. J. Villas-Boas, R. Kaiser, and R. Bachelard, Generating long-lived entangled states with free-space collective spontaneous emission, Phys. Rev. A **105**, 053715 (2022).

[32] O. Rubies-Bigorda, S. Ostermann, and S. F. Yelin, Generating multi-excitation subradiant states in incoherently excited atomic arrays, arXiv:2209.00034 (2022).

[33] N. Skribanowitz, I. P. Herman, J. C. MacGillivray, and M. S. Feld, Observation of Dicke superradiance in optically pumped HF gas, Phys. Rev. Lett. **30**, 309 (1973).

[34] A. Flusberg, T. Mossberg, and S. Hartmann, Observation of Dicke superradiance at 1.30 μm in atomic Tl vapor, Physics Letters A **58**, 373 (1976).

[35] M. Gross, C. Fabre, P. Pillet, and S. Haroche, Observation of near-infrared Dicke superradiance on cascading transitions in atomic sodium, Phys. Rev. Lett. **36**, 1035 (1976).

[36] Q. H. F. Vrehen, H. M. J. Hikspoors, and H. M. Gibbs, Quantum beats in superfluorescence in atomic cesium, Phys. Rev. Lett. **38**, 764 (1977).

[37] F. Gounand, M. Hugon, P. R. Fournier, and J. Berlande, Superradiant cascading effects in rubidium Rydberg levels, Journal of Physics B: Atomic and Molecular Physics **12**, 547 (1979).

[38] F. Meinardi, M. Cerminara, A. Sassella, R. Bonifacio, and R. Tubino, Superradiance in molecular H aggregates, Phys. Rev. Lett. **91**, 247401 (2003).

[39] M. Scheibner, T. Schmidt, L. Worschech, A. Forchel, G. Bacher, T. Passow, and D. Hommel, Superradiance of quantum dots, Nature Physics **3**, 106 (2007).

[40] G. Rainò, M. A. Becker, M. I. Bodnarchuk, R. F. Mahrt, M. V. Kovalenko, and T. Stöferle, Superfluorescence from lead halide perovskite quantum dot superlattices, Nature **563**, 671 (2018).

[41] G. Ferioli, A. Glicenstein, F. Robicheaux, R. T. Sutherland, A. Browaeys, and I. Ferrier-Barbut, Laser-driven superradiant ensembles of two-level atoms near Dicke regime, Phys. Rev. Lett. **127**, 243602 (2021).

[42] W. S. Bakr, A. Peng, M. E. Tai, R. Ma, J. Simon, J. I. Gillen, S. Fölling, L. Pollet, and M. Greiner, Probing the superfluid–to–Mott insulator transition at the single-atom level, Science **329**, 547 (2010).

[43] J. F. Sherson, C. Weitenberg, M. Endres, M. Cheneau, I. Bloch, and S. Kuhr, Single-atom-resolved fluorescence imaging of an atomic Mott insulator, Nature **467**, 68 (2010).

[44] H. Kim, W. Lee, H.-G. Lee, H. Jo, Y. Song, and J. Ahn, In situ single-atom array synthesis using dynamic holographic optical tweezers, Nat. Commun. **7**, 13317 (2016).

[45] M. Endres, H. Bernien, A. Keesling, H. Levine, E. R. Anschuetz, A. Krajenbrink, C. Senko, V. Vuletic, M. Greiner, and M. D. Lukin, Atom-by-atom assembly of defect-free one-dimensional cold atom arrays, Science **354**, 1024 (2016).

[46] D. Barredo, S. de Léséleuc, V. Lienhard, T. Lahaye, and A. Browaeys, An atom-by-atom assembler of defect-free arbitrary two-dimensional atomic arrays, Science **354**, 1021 (2016).

[47] A. Kumar, T.-Y. Wu, F. Giraldo, and D. S. Weiss, Sorting ultracold atoms in a three-dimensional optical lattice in a realization of Maxwell's demon, Nature **561**, 83 (2018).

[48] S. J. Masson and A. Asenjo-Garcia, Universality of Dicke superradiance in arrays of quantum emitters, Nat. Commun. **13**, 2285 (2022).

[49] E. Sierra, S. J. Masson, and A. Asenjo-Garcia, Dicke superradiance in ordered lattices: Dimensionality matters, Phys. Rev. Research **4**, 023207 (2022).

[50] F. Robicheaux, Theoretical study of early-time superradiance for atom clouds and arrays, Phys. Rev. A **104**, 063706 (2021).

[51] O. Rubies-Bigorda and S. F. Yelin, Superradiance and subradiance in inverted atomic arrays, Phys. Rev. A **106**, 053717 (2022).

[52] W. F. Meggers and J. L. Tech, The first spectrum of ytterbium (Yb I), J. Res. Natl. Bur. Stand. **83**, 13 (1978).

[53] S. G. Porsev, Y. G. Rakhlina, and M. G. Kozlov, Electric-dipole amplitudes, lifetimes, and polarizabilities of the low-lying levels of atomic ytterbium, Phys. Rev. A **60**, 2781 (1999).

[54] P. G. Mickelson, Y. N. Martinez de Escobar, P. Anzel, B. J. DeSalvo, S. B. Nagel, A. J. Traverso, M. Yan, and T. C. Killian, Repumping and spectroscopy of laser-cooled Sr atoms using the $(5s5p)^3P_2$-$(5s4d)^3D_2$ transition, J. Phys. B **42**, 235001 (2009).

[55] J. E. Sansonetti and G. Nave, Wavelengths, transition probabilities, and energy levels for the spectrum of neutral strontium (Sr I), J. Phys. Chem. Ref. Data **39**, 033103 (2010).

[56] S. Zhang, P. Ramchurn, M. Menchetti, Q. Ubaid, J. Jones, K. Bongs, and Y. Singh, Novel repumping on $^3P_0 \rightarrow {}^3D_1$ for Sr magneto-optical trap and Landé g factor measurement of $^3D_1$, J. Phys. B **53**, 235301 (2020).

[57] W. Bowden, R. Hobson, I. R. Hill, A. Vianello, M. Schioppo, A. Silva, H. S. Margolis, P. E. G. Baird, and P. Gill, A pyramid MOT with integrated optical cavities as a cold atom platform for an optical lattice clock, Sci. Rep. **9**, 11704 (2019).

[58] B. Olmos, D. Yu, Y. Singh, F. Schreck, K. Bongs, and I. Lesanovsky, Long-range interacting many-body systems with alkaline-earth-metal atoms, Phys. Rev. Lett. **110**, 143602 (2013).

[59] A. D. Ludlow, T. Zelevinsky, G. K. Campbell, S. Blatt, M. M. Boyd, M. H. G. de Miranda, M. J. Martin, J. W. Thomsen, S. M. Foreman, J. Ye, T. M. Fortier, J. E. Stalnaker, S. A. Diddams, Y. Le Coq, Z. W. Barber, N. Poli, N. D. Lemke, K. M. Beck, and C. W. Oates, Sr lattice clock at 1×10^{-16} fractional uncertainty by remote optical evaluation with a Ca clock, Science **319**, 1805 (2008).

[60] N. Hinkley, J. A. Sherman, N. B. Phillips, M. Schioppo, N. D. Lemke, K. Beloy, M. Pizzocaro, C. W. Oates, and A. D. Ludlow, An atomic clock with 10^{-18} instability, Science **341**, 1215 (2013).

[61] B. J. Bloom, T. L. Nicholson, J. R. Williams, S. L. Campbell, M. Bishof, X. Zhang, W. Zhang, S. L. Bromley, and J. Ye, An optical lattice clock with accuracy and stability at the 10^{-18} level, Nature **506**, 71 (2014).

[62] I. Ushijima, M. Takamoto, M. Das, T. Ohkubo, and H. Katori, Cryogenic optical lattice clocks, Nat. Photon. **9**, 185 (2015).

[63] N. Nemitz, T. Ohkubo, M. Takamoto, I. Ushijima, M. Das, N. Ohmae, and H. Katori, Frequency ratio of Yb and Sr clocks with 5×10^{-17} uncertainty at 150 seconds averaging time, Nat. Photon. **10**, 258 (2016).

[64] M. Schioppo, R. C. Brown, W. F. McGrew, N. Hinkley, R. J. Fasano, K. Beloy, T. H. Yoon, G. Milani, D. Nicolodi, J. A. Sherman, N. B. Phillips, C. W. Oates, and A. D. Ludlow, Ultrastable optical clock with two cold-atom ensembles, Nat. Photon. **11**, 48 (2017).

[65] S. B. Koller, J. Grotti, S. Vogt, A. Al-Masoudi, S. Dörscher, S. Häfner, U. Sterr, and C. Lisdat, Transportable optical lattice clock with 7×10^{-17} uncertainty, Phys. Rev. Lett. **118**, 073601 (2017).

[66] I. S. Madjarov, A. Cooper, A. L. Shaw, J. P. Covey, V. Schkolnik, T. H. Yoon, J. R. Williams, and M. Endres, An atomic-array optical clock with single-atom readout, Phys. Rev. X **9**, 041052 (2019).

[67] A. W. Young, W. J. Eckner, W. R. Milner, D. Kedar, M. A. Norcia, E. Oelker, N. Schine, J. Ye, and A. M. Kaufman, Half-minute-scale atomic coherence and high relative stability in a tweezer clock, Nature **588**, 408 (2020).

[68] A. J. Daley, M. M. Boyd, J. Ye, and P. Zoller, Quantum computing with alkaline-earth-metal atoms, Phys. Rev. Lett. **101**, 170504 (2008).

[69] A. V. Gorshkov, A. M. Rey, A. J. Daley, M. M. Boyd, J. Ye, P. Zoller, and M. D. Lukin, Alkaline-earth-metal atoms as few-qubit quantum registers, Phys. Rev. Lett. **102**, 110503 (2009).

[70] N. Chen, L. Li, W. Huie, M. Zhao, I. Vetter, C. H. Greene, and J. P. Covey, Analyzing the Rydberg-based optical-metastable-ground architecture for ^{171}Yb nuclear spins, Phys. Rev. A **105**, 052438 (2022).

[71] Y. Wu, S. Kolkowitz, S. Puri, and J. D. Thompson, Erasure conversion for fault-tolerant quantum computing in alkaline earth Rydberg atom arrays, Nat. Commun. **13**, 4657 (2022).

[72] A. Cooper, J. P. Covey, I. S. Madjarov, S. G. Porsev, M. S. Safronova, and M. Endres, Alkaline-earth atoms in optical tweezers, Phys. Rev. X **8**, 041055 (2018).

[73] M. A. Norcia, A. W. Young, and A. M. Kaufman, Microscopic control and detection of ultracold strontium in optical-tweezer arrays, Phys. Rev. X **8**, 041054 (2018).

[74] K. Barnes, P. Battaglino, B. J. Bloom, K. Cassella, R. Coxe, N. Crisosto, J. P. King, S. S. Kondov, K. Kotru, S. C. Larsen, J. Lauigan, B. J. Lester, M. McDonald, E. Megidish, S. Narayanaswami, C. Nishiguchi, R. Notermans, L. S. Peng, A. Ryou, T.-Y. Wu, and M. Yarwood, Assembly and coherent control of a register of nuclear spin qubits, Nat. Commun. **13**, 2779 (2022).

[75] S. Saskin, J. T. Wilson, B. Grinkemeyer, and J. D. Thompson, Narrow-line cooling and imaging of ytterbium atoms in an optical tweezer array, Phys. Rev. Lett. **122**, 143002 (2019).

[76] A. Jenkins, J. Lis, A. Senoo, W. McGrew, and A. Kaufman, Ytterbium nuclear-spin qubits in an optical tweezer array, Phys. Rev. X **12**, 021027 (2022).

[77] D. Okuno, Y. Nakamura, T. Kusano, Y. Takasu, N. Takei, H. Konishi, and Y. Takahashi, High-resolution spectroscopy and single-photon Rydberg excitation of reconfigurable ytterbium atom tweezer arrays utilizing a metastable state, J. Phys. Soc. Jpn. **91**, 084301 (2022).

[78] S. Ma, A. P. Burgers, G. Liu, J. Wilson, B. Zhang, and J. D. Thompson, Universal gate operations on nuclear spin qubits in an optical tweezer array of ^{171}Yb atoms, Phys. Rev. X **12**, 021028 (2022).

[79] M. Miranda, R. Inoue, Y. Okuyama, A. Nakamoto, and M. Kozuma, Site-resolved imaging of ytterbium atoms in a two-dimensional optical lattice, Phys. Rev. A **91**, 063414 (2015).

[80] R. Yamamoto, J. Kobayashi, T. Kuno, K. Kato, and Y. Takahashi, An ytterbium quantum gas microscope with narrow-line laser cooling, New J. Phys. **18**, 023016 (2016).

[81] J. P. Covey, A. Sipahigil, S. Szoke, N. Sinclair, M. Endres, and O. Painter, Telecom-band quantum optics with ytterbium atoms and silicon nanophotonics, Phys. Rev. Applied **11**, 034044 (2019).

[82] J. P. Covey, A. Sipahigil, and M. Saffman, Microwave-to-optical conversion via four-wave mixing in a cold ytterbium ensemble, Phys. Rev. A **100**, 012307 (2019).

[83] W. Huie, S. G. Menon, H. Bernien, and J. P. Covey, Multiplexed telecommunication-band quantum networking with atom arrays in optical cavities, Phys. Rev. Res. **3**, 043154 (2021).

[84] D. P. Fahey and M. W. Noel, Excitation of Rydberg states in rubidium with near infrared diode lasers, Opt. Express **19**, 17002 (2011).

[85] P. J. Moran, R. M. Richards, C. A. Rice, and G. P. Perram, Near infrared rubidium $6^2P_{3/2,1/2} \rightarrow 6^2S_{1/2}$ laser, Opt. Commun. **374**, 51 (2016).

[86] M. Uphoff, M. Brekenfeld, G. Rempe, and S. Ritter, An integrated quantum repeater at telecom wavelength with single atoms in optical fiber cavities, Appl. Phys. B **122**, 46 (2016).

[87] S. G. Menon, K. Singh, J. Borregaard, and H. Bernien, Nanophotonic quantum network node with neutral atoms and an integrated telecom interface, New J. Phys. **22**, 073033 (2020).

[88] G.-D. Lin and S. F. Yelin, Superradiance in spin-j particles: Effects of multiple levels, Phys. Rev. A **85**, 033831 (2012).

[89] R. T. Sutherland and F. Robicheaux, Superradiance in inverted multilevel atomic clouds, Phys. Rev. A **95**, 033839 (2017).

[90] T. Gruner and D.-G. Welsch, Green-function approach to the radiation-field quantization for homogeneous and inhomogeneous Kramers-Kronig dielectrics, Phys. Rev. A **53**, 1818 (1996).

[91] H. T. Dung, L. Knöll, and D.-G. Welsch, Resonant dipole-dipole interaction in the presence of dispersing and absorbing surroundings, Phys. Rev. A **66**, 063810 (2002).

[92] A. Asenjo-Garcia, J. D. Hood, D. E. Chang, and H. J. Kimble, Atom-light interactions in quasi-one-dimensional nanostructures: A Green's-function perspective, Phys. Rev. A **95**, 033818 (2017).

[93] H. J. Carmichael and K. Kim, A quantum trajectory unraveling of the superradiance master equation, Opt. Commun. **179**, 417 (2000).

[94] S. Krämer and H. Ritsch, Generalized mean-field approach to simulate the dynamics of large open spin ensembles with long range interactions, Eur. Phys. J. D **69**, 282 (2015).

[95] F. Robicheaux and D. A. Suresh, Beyond lowest order mean-field theory for light interacting with atom arrays, Phys. Rev. A **104**, 023702 (2021).

[96] O. Rubies-Bigorda, S. Ostermann, and S. F. Yelin, Characterizing superradiant dynamics in atomic arrays via a cumulant expansion approach, arXiv:2209.00034 (2022).

[97] Y. Ma, R. Liu, L. Ji, L. Qiu, S. Wu, D. Su, Y. Zhao, N. Yao, and W. Fang, Composite picosecond control of atomic state through a nanofiber interface, arXiv:2203.06716 10.48550/ARXIV.2203.06716 (2022).

[98] A. Asenjo-Garcia, H. J. Kimble, and D. E. Chang, Optical waveguiding by atomic entanglement in multilevel atom arrays, Proc. Natl. Acad. Sci. USA **116**, 25503 (2019).

[99] G. Nienhuis and F. Schuller, Spontaneous emission and light scattering by atomic lattice models, J. Phys. B **20**, 23 (1987).

[100] R. J. Bettles, S. A. Gardiner, and C. S. Adams, Cooperative eigenmodes and scattering in one-dimensional atomic arrays, Phys. Rev. A **94**, 043844 (2016).

[101] R. Asaoka, J. Gea-Banacloche, Y. Tokunaga, and K. Koshino, Stimulated emission of superradiant atoms in waveguide quantum electrodynamics, Phys. Rev. Appl. **18**, 064006 (2022).

[102] W. Kersten, N. de Zordo, O. Diekmann, T. Reiter, M. Zens, A. N. Kanagin, S. Rotter, J. Schmiedmayer, and A. Angerer, Triggered superradiance and inversion storage in a hybrid quantum system (2023).

[103] S. Kraft, F. Vogt, O. Appel, F. Riehle, and U. Sterr, Bose-Einstein condensation of alkaline earth atoms:

^{40}Ca, Phys. Rev. Lett. **103**, 130401 (2009).

[104] S. De, U. Dammalapati, K. Jungmann, and L. Willmann, Magneto-optical trapping of barium, Phys. Rev. A **79**, 041402 (2009).

[105] R. H. Parker, M. R. Dietrich, K. Bailey, J. P. Greene, R. J. Holt, M. R. Kalita, W. Korsch, Z.-T. Lu, P. Mueller, T. P. O'Connor, J. Singh, I. A. Sulai, and W. L. Trimble, Efficient, tightly-confined trapping of ^{226}Ra, Phys. Rev. C **86**, 065503 (2012).

[106] A. P. Kulosa, D. Fim, K. H. Zipfel, S. Rühmann, S. Sauer, N. Jha, K. Gibble, W. Ertmer, E. M. Rasel, M. S. Safronova, U. I. Safronova, and S. G. Porsev, Towards a Mg lattice clock: Observation of the $^1S_0$–$^3P_0$ transition and determination of the magic wavelength, Phys. Rev. Lett. **115**, 240801 (2015).

[107] J. R. Guest, N. D. Scielzo, I. Ahmad, K. Bailey, J. P. Greene, R. J. Holt, Z.-T. Lu, T. P. O'Connor, and D. H. Potterveld, Laser trapping of ^{225}Ra and ^{226}Ra with repumping by room-temperature blackbody radiation, Phys. Rev. Lett. **98**, 093001 (2007).

[108] M. Lu, N. Q. Burdick, S. H. Youn, and B. L. Lev, Strongly dipolar Bose-Einstein condensate of dysprosium, Phys. Rev. Lett. **107**, 190401 (2011).

[109] K. Aikawa, A. Frisch, M. Mark, S. Baier, A. Rietzler, R. Grimm, and F. Ferlaino, Bose-einstein condensation of erbium, Phys. Rev. Lett. **108**, 210401 (2012).

[110] B. Hemmerling, G. K. Drayna, E. Chae, A. Ravi, and J. M. Doyle, Buffer gas loaded magneto-optical traps for Yb, Tm, Er and Ho, New J. Phys. **16**, 063070 (2014).

[111] J. Miao, J. Hostetter, G. Stratis, and M. Saffman, Magneto-optical trapping of holmium atoms, Phys. Rev. A **89**, 041401 (2014).

[112] H. Labuhn, D. Barredo, S. Ravets, S. de Léséleuc, T. Macrì, T. Lahaye, and A. Browaeys, Tunable two-dimensional arrays of single Rydberg atoms for realizing quantum Ising models, Nature **534**, 667 (2016).

[113] H. Bernien, S. Schwartz, A. Keesling, H. Levine, A. Omran, H. Pichler, S. Choi, A. S. Zibrov, M. Endres, M. Greiner, V. Vuletić, and M. D. Lukin, Probing many-body dynamics on a 51-atom quantum simulator, Nature **551**, 579 (2017).

[114] A. Browaeys and T. Lahaye, Many-body physics with individually controlled Rydberg atoms, Nat. Phys. **16**, 132 (2020).

[115] T. Wang, S. F. Yelin, R. Côté, E. E. Eyler, S. M. Farooqi, P. L. Gould, M. Koštrun, D. Tong, and D. Vrinceanu, Superradiance in ultracold Rydberg gases, Phys. Rev. A **75**, 033802 (2007).

[116] E. A. Goldschmidt, T. Boulier, R. C. Brown, S. B. Koller, J. T. Young, A. V. Gorshkov, S. L. Rolston, and J. V. Porto, Anomalous broadening in driven dissipative Rydberg systems, Phys. Rev. Lett. **116**, 113001 (2016).

[117] K. Beloy, J. A. Sherman, N. D. Lemke, N. Hinkley, C. W. Oates, and A. D. Ludlow, Determination of the $5d6s\ ^3D_1$ state lifetime and blackbody-radiation clock shift in Yb, Phys. Rev. A **86**, 051404 (2012).

[118] T. L. Nicholson, S. L. Campbell, R. B. Hutson, G. E. Marti, B. J. Bloom, R. L. McNally, W. Zhang, M. D. Barrett, M. S. Safronova, G. F. Strouse, W. L. Tew, and J. Ye, Systematic evaluation of an atomic clock at 2×10^{-18} total uncertainty, Nat. Commun. **6**, 6896 (2015).

[119] R. B. Hutson, W. R. Milner, L. Yan, J. Ye, and C. Sanner, Observation of mHz-level cooperative Lamb shifts in an optical atomic clock, arXiv:2303.05613 (2023).

[120] O. Rubies-Bigorda, V. Walther, T. L. Patti, and S. F. Yelin, Photon control and coherent interactions via lattice dark states in atomic arrays, Phys. Rev. Research **4**, 013110 (2022).

[121] V. Paulisch, H. J. Kimble, and A. González-Tudela, Universal quantum computation in waveguide QED using decoherence free subspaces, New J. Phys. **18**, 043041 (2016).

[122] L. Henriet, J. S. Douglas, D. E. Chang, and A. Albrecht, Critical open-system dynamics in a one-dimensional optical-lattice clock, Phys. Rev. A **99**, 023802 (2019).

[123] H. J. Carmichael, *An Open Systems Approach to Quantum Optics*, Lecture Notes in Physics, Vol. 18 (Springer-Verlag Berlin Heidelberg, 1993).